

**Sensitivity of L-band passive microwaves to carbon stocks in tropical forests: a comparison to  
higher microwave frequencies and optical data**

David Chaparro<sup>1,\*</sup>, Grégory Duveiller<sup>2</sup>, Maria Piles<sup>3</sup>, Alessandro Cescatti<sup>2</sup>, Mercè Vall-Ilossera<sup>1</sup>,  
Adriano Camps<sup>1</sup>, Dara Entekhabi<sup>4</sup>

\*Corresponding author: [david.chaparro@tsc.upc.edu](mailto:david.chaparro@tsc.upc.edu)

<sup>1</sup> Universitat Politècnica de Catalunya, CommSensLab & IEEC/UPC, Jordi Girona 1-3, E-08034,  
Barcelona, Spain.

<sup>2</sup> European Commission, Joint Research Centre, Directorate for Sustainable Resources, Ispra, Italy.

<sup>3</sup> Image Processing Lab (IPL), Universitat de València, 46980, Valencia, Spain.

<sup>4</sup> Department of Civil and Environmental Engineering, Massachusetts Institute of Technology,  
Cambridge, MA 02139, United States.

## **Abstract**

Monitoring vegetation carbon in tropical regions is essential to the global carbon assessment and to evaluate the actions oriented to the reduction of forest degradation. Mainly, satellite optical vegetation indices and LiDAR data have been used to this purpose. These two techniques are limited by cloud cover and are sensitive only to the top of vegetation. In addition, the vegetation attenuation to the soil microwave emission, represented by the vegetation optical depth (VOD), has been applied for biomass estimation using frequencies ranging from 4 to 30 GHz (C- to K-bands). Atmosphere is transparent to microwaves and their sensitivity to canopy layers depends on the frequency, with lower frequencies having greater penetration depths. In this regard, L-band VOD (1.4 GHz) is expected to enhance the ability to estimate carbon stocks. This study compares the sensitivity of different VOD products (from L, C, and X-bands) and an optical vegetation index (EVI) to the above-ground carbon density (ACD). It quantifies the contribution of ACD and forest cover proportion to the VOD/EVI signals. The study is conducted in Peru, southern Colombia and Panama, where ACD maps have been derived from airborne LiDAR. Results confirm the enhanced sensitivity of L-band VOD to ACD when compared to higher frequency bands, and show that the sensitivity of all VOD bands decreases in the densest forests. ACD explains 34% and forest cover 30% of L-band VOD variance, and these proportions gradually decrease for EVI, C-, and X-band VOD, respectively. Results are consistent through different categories of altitude and carbon density. This pattern is found in most of the studied regions and in flooded forests. Results also show that C-, X-band VOD and EVI provide complementary information to L-band VOD, especially in flooded forests and in mountains, indicating that synergistic approaches could lead to improved retrievals in these regions. Although the assessment of vegetation carbon in the densest forests requires further research, results from this study support the use of new L-band VOD estimates for mapping the carbon of tropical forests.

**Keywords:** Vegetation optical depth, carbon density, tropical forests, L-band, climate change.

## **1. Introduction**

Control and mitigation of climate change greatly depend on the carbon balance of land ecosystems, and in particular on the capacity of tropical forests to store large amounts of carbon. Intact tropical forests (i.e., not affected by human activities) are responsible of half of the carbon sequestration in woodlands across the world (Pan et al., 2011), but deforestation, forest degradation, and disturbances in tropical regions counteract this effect causing tropical forests to be a net carbon source (Pan et al., 2011; Liu et al., 2015; Baccini et al., 2017). Despite this fact, terrestrial ecosystems act as global and significant carbon sinks, although the sink strengths' show large variability among years and its future dynamic is uncertain (Le Quéré et al., 2009 and 2016). In this context, monitoring the land carbon stocks at global scale is essential to assess the carbon budget, reduce uncertainties, gain precision on modelling future climate change scenarios, and ultimately contribute to the development of effective climate change mitigation strategies.

Satellites are the only means to provide an efficient and cost-effective monitoring of vegetation biomass changes over large areas and over extended periods (Goetz et al., 2009). Previous research on biomass estimation from space observations has been frequently based on the combination of diverse remote sensing sources and on complementing satellite data with field plots. The most widely used technique for vegetation monitoring is based on visible-infrared (VIS/NIR) vegetation indices. These indices have been constructed to exploit the particular properties of green vegetation to strongly absorb red wavelengths and reflect in the near-infrared. Several studies have used such indices for biomass estimation. For example, data from the Moderate Resolution Imaging Spectroradiometer (MODIS) have been applied to map carbon density in tropical regions (Baccini et al., 2008; Baccini et al., 2017) and in China (Sun et al., 2015). Spectral vegetation indices, such as the Normalized Difference Vegetation Index (NDVI) and the Enhanced Vegetation Index (EVI), have also been combined with field measurements to estimate forest biomass (e.g., Myneni et al., 2001; Dong

et al., 2003; González-Alonso et al., 2006; Blackard et al., 2008; Yuan et al., 2016). Despite their importance on vegetation studies, VIS/NIR vegetation indices have serious limitation for monitoring carbon stocks because they (i) are masked by clouds, (ii) can only monitor the top of the vegetation canopy, thus saturating at moderate and high levels of vegetation densities, and (iii) are poorly related to aboveground biomass.

Differently from –and complementarily to- the VIS/NIR datasets, optical remote sensing based on the emission of laser pulses (i.e., light detection and ranging; LiDAR) presents the unique advantage of capturing the vertical structure of vegetation. It can be used to map the forest height and architecture in detail. The application of LiDAR enhances the capacity to capture vegetation biomass at different spatial scales. In that sense, new estimations of biomass and carbon fluxes throughout the Earth tropical regions have been obtained merging LiDAR satellite data with MODIS information and/or microwave datasets (Saatchi et al., 2011; Baccini et al., 2012 and 2017). At present, LiDAR surveys of forest biomass are limited to airborne platforms, although the Ice, Cloud, and land Elevation Satellite (ICESat) provided LiDAR measurements between 2003 and 2009. ICESat data was used for mapping forest canopy height (Simard et al., 2011), and future satellite missions like the ICESat-2 and the Global Ecosystem Dynamics Investigation mission (GEDI) will produce LiDAR retrievals of canopy structure from space. Importantly for the scope of this work, airborne LiDAR from the Carnegie Airborne Observatory (CAO) –in combination with field and modelled datasets- has been used to produce above-ground carbon density (ACD) maps at regional scales in Peru, southern Colombia and Panama (Asner et al., 2012, 2013 and 2014).

Microwave remote sensing, either from active or passive sensors (i.e., radars or radiometers, respectively), provides an alternative technique that has a double advantage: it is insensitive to cloud cover, and it is able to sense the vegetation (at different layers and depths depending on the frequency). Microwave sensors are responsive to the water content of soils and vegetation (i.e., soil

moisture and vegetation water content, respectively). This is due to the fact that water changes the dielectric properties of land covers as well as the attenuation, emission and reflection of vegetation layers and soils at microwave frequencies. In order to derive biomass estimates, it is assumed that the vegetation water content (VWC) to which microwaves are sensitive is tightly linked to the biomass of the plant. The relationship between measurements from space-borne radars and biomass in tropical forests has been widely demonstrated (Luckman et al., 1997; Kuplich et al., 2010; Hamdan et al., 2011; Morel et al., 2011; Häme et al., 2013; Sinha et al., 2015; Viet Nguyen et al., 2016). Radar data have been used to provide vegetation biomass estimates either in synergy with LiDAR and VIS/NIR data (Saatchi et al., 2007; Lucas et al., 2015) or as an independent data source (Thurner et al., 2014; Bouvet et al., 2018). The use of passive microwave measurements for biomass assessments relies on the estimation of a physical microwave parameter known as Vegetation Optical Depth (VOD). This variable represents the attenuation exerted by the vegetation over soil microwave emissions, which depends on the VWC (Ulaby et al., 1986, pp. 1551-1596; Jackson and Schmugge, 1991; Momen et al., 2017), and therefore is used as a proxy of biomass. Different VOD products have been applied to study forests conditions and biomass (Liu et al., 2013; Lucas et al., 2015; van Marle et al., 2016; Brandt et al., 2017). In particular, trends in global terrestrial biomass have been estimated using long-term retrievals of VOD at C-, X- and K-bands (>4 GHz; Liu et al., 2011 and 2015). In this regard, since the penetration depth of microwaves through the vegetation canopy is greater at lower frequencies, VOD at L-band (1 to 2 GHz) is representative of the amount of water within most of the above-ground vegetation canopy, and SM and VOD retrievals can be successfully performed under denser vegetation conditions than those sensed by higher frequency bands. Hence, L-band is expected to enhance the capacity to derive information on vegetation for a wide range of applications.

At present, there are two L-band passive microwave satellite missions in orbit. The ESA's Soil Moisture and Ocean Salinity (SMOS) mission (launched in November 2009) has on-board a synthetic aperture interferometric radiometer providing full-polarimetric measurements at different incidence angles (Kerr et al., 2010). The NASA's Soil Moisture Active Passive (SMAP) satellite (launched in January 2015) has a single-look angle radiometer and a synthetic aperture radar on-board (Entekhabi et al., 2010). The SMAP's radar aimed at providing higher resolution soil moisture estimates, but it failed after three months of operations. At present, the SMOS VOD datasets include L2 and L3 products (Kerr et al., 2012; Al-Bitar et al., 2017) as well as the SMOS-INRA-CESBIO dataset (SMOS-IC; Fernández-Moran et al., 2017). The SMAP VOD products derive from the dual-channel baseline algorithm (SMAP DCA) and from the Multi-temporal Dual Channel Algorithm (SMAP MT-DCA; Konings et al., 2016).

L-band VOD datasets have been used in vegetation research to study Gross Primary Production (GPP; Teubner et al., 2018) and crop yields (Chaparro et al., 2018). L-band VOD has shown good agreement with vegetation biomass and forest height (Vittucci et al., 2016a and 2016b; Konings, Piles, et al., 2017). Brandt et al. (2018) have demonstrated its applicability to monitor carbon dynamics associated to weather trends in African drylands, and have shown reduced saturation for L-band VOD at high values of vegetation biomass compared to higher frequency (shorter wavelength) microwaves. Vittucci et al. (2016b) have reported that in July 2015 L-band VOD showed stronger relationship with biomass and forest height than C-band VOD in tropical forests of South America and Africa. However, they have found low relationship of L- and C-bands VOD with biomass in Indonesian forests, with similar performance for biomass estimation at both frequencies. In this context, further work is needed to quantify and compare the relationship between above-ground carbon stocks and VOD at different frequencies and for different forest types. At present it is

still unclear to what extent L-band VOD shows higher sensitivity to capture carbon patterns than other frequency bands and vegetation indices.

The main goal of this study is to assess and compare the sensitivity of VOD (at L-, C- and X-bands) to above-ground carbon density (ACD), as well as to compare it with EVI. The study is conducted with a principal focus on tropical forests in Peru, southern Colombia and Panama, and is structured in two parts. Firstly, the relationship between satellite VOD and ACD derived from airborne LiDAR surveys is established and analysed. This shows the effect of vegetation density on the L-band VOD signal and compares it to the different microwave frequencies. A relationship between the VOD-ACD regression residuals and different geographical features in the region is also presented. Secondly, the relative contribution of ACD and forest cover (FC) fraction to the VOD signal is studied. This allows understanding to what extent the VOD could depend on the changing forest cover within a region rather than on the carbon density variability *per se*. In this second part, the EVI is included to complement the study. Its dependence on ACD and FC is also presented and compared to VOD. The analyses are specifically reproduced for the Andes Mountains and for the flooded forests found in the study area, which exhibit distinct VOD-ACD relationships and vegetation patterns.

## **2. Materials and methods**

### **2.1. Study area**

The limits of the study area (Figure 1) are based on the availability of ACD maps. It encompasses Peru (~1.3 million km<sup>2</sup>), Panama (~75,000 km<sup>2</sup>) and part of the Colombian Amazon (~165,000 km<sup>2</sup>).

Peru and southern Colombia contain the Amazon basin, crossed by the Amazon River and its tributaries. In western Peru, the Andes Mountains reach altitudes above 6,500 m.

The evergreen tropical rainforests in the region are the main target of this study. Near some rivers edges, and particularly in north-central Peru, these forests are flooded forests (Figure 1a). The Amazonian forests constitute one of the main land carbon reservoirs on Earth. Other land covers are found in the Andes, where a transition from dense forests to shrublands, grasslands, and bare soils is found successively with increasing altitudes. Also, croplands, shrublands and grasslands are present in the north of the studied area of Colombia and in western Panama (Figure 1a).

## 2.2. Datasets

### *2.2.1. Above-ground Carbon Density (ACD)*

The Above-ground Carbon Density (ACD) maps produced by the Carnegie Airborne Observatory (CAO; Asner et al., 2012, 2013 and 2014) are used as a benchmark to assess the sensitivity of remote sensing datasets to the variability of carbon stocks. The ACD dataset is based on intensive airborne LiDAR sampling carried out between years 2011 and 2012. LiDAR measurements are converted to top-of-canopy height (TCH) information which, in turn, is transformed to ACD data (100 m resolution) using calibration against field plots and information on topography, vegetation and precipitation. ACD ranges between 0 and 140 TC/ha in the study area. The degree of uncertainty at the original ACD resolution reaches up to 28.3% in Colombia and 23% in Panama. This is computed in terms of error relative to the mean. In the case of Peru, the uncertainty in the vast majority of the tropical forest area is below 10%. It may increase in flooded forests and river areas ranging from <5% to 50% in most of these regions. Errors around 80% are found in the Andes, but this is largely due to the fact that the mean ACD values per pixel are close to zero in this area, causing large relative uncertainties



with low ACD absolute errors. More details on the ACD dataset are provided in Asner et al. 2012 (Colombia), 2013 (Panama), and 2014 (Peru). In this work, the ACD dataset is aggregated to 25 km scale to match the spatial scale of other data layers, and is shown in Figure 1b.

### *2.2.2. Vegetation Optical Depth*

The L-band (1.4 GHz) VOD is derived from the NASA's Soil Moisture Active-Passive (SMAP) satellite, which has a revisit time of 3 days and a native resolution of approximately 36 km. The SMAP single-look incidence angle configuration limits the capability to extract VOD information with just one acquisition (Konings et al., 2015 and 2016). Therefore, the Multi-Temporal Dual-Channel Algorithm (MT-DCA) is proposed to estimate soil moisture and VOD from single look-angle observations using two consecutive overpasses and no ancillary information on vegetation (Konings et al., 2016). SMAP VOD datasets retrieved using MT-DCA have shown good agreement with vegetation and land cover patterns at global scale (Konings, Piles, et al., 2017). Here, the first year of SMAP VOD data (April 2015 - March 2016) is used. This dataset is retrieved from SMAP Backus-Gilbert enhanced brightness temperatures using the MT-DCA and is provided in the 9 km EASE 2.0 grid (NSIDC, 2017). It has been aggregated to 25 km (obtained using bilinear interpolation; Figure 1c) for comparison with the higher frequency VOD bands at their available grid scale (see below), and with EVI.

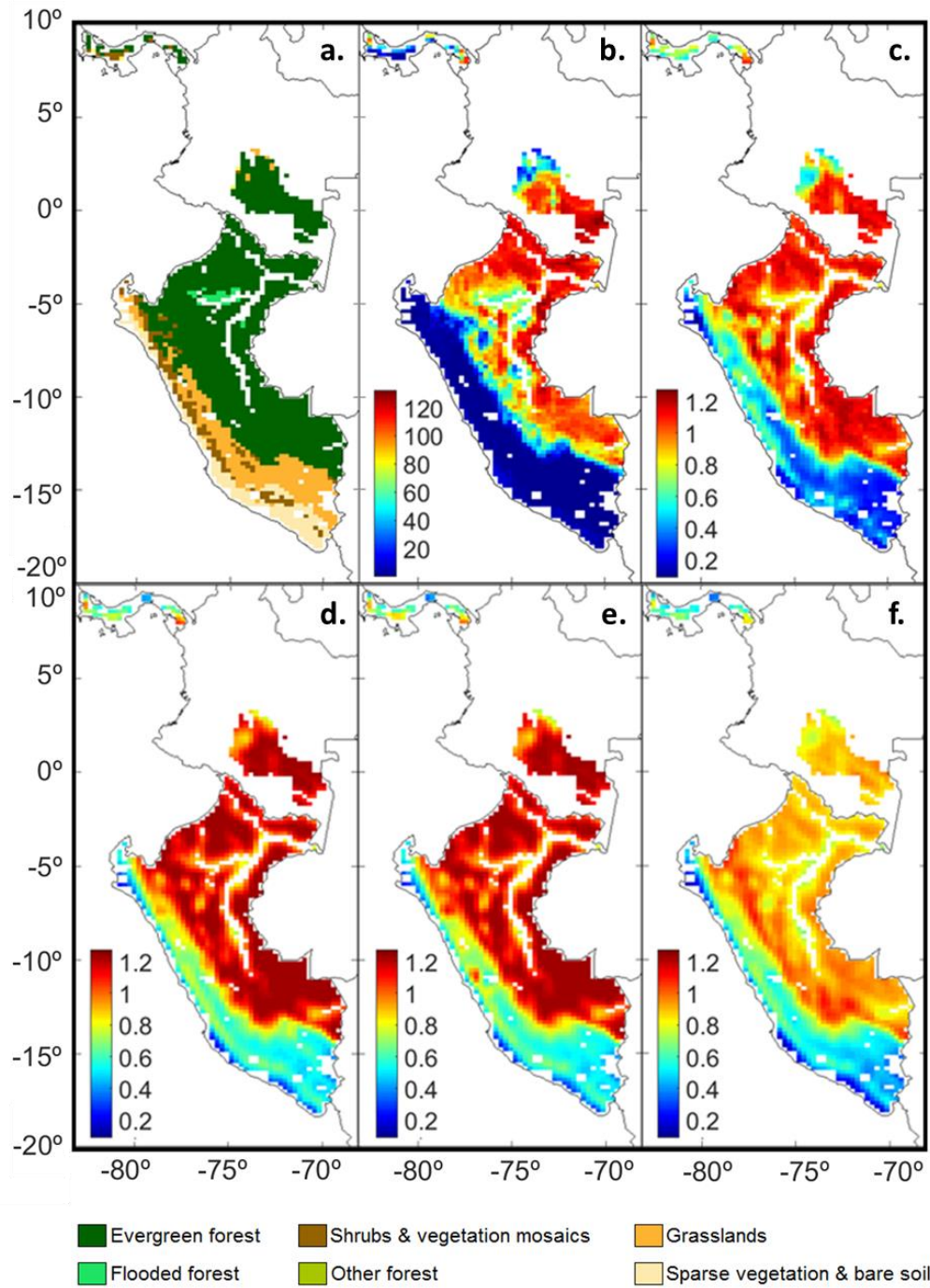


**Figure 1.** The study area includes Panama, southern Colombia, and Peru. a) Land Cover mode for the year 2015 (ESA-CCI, 2017); b) Above-ground Carbon Density (TC/ha); c) Mean L-band VOD (1.4 GHz; SMAP); d) Mean C1-band VOD (6.9 GHz; AMSR2); e) Mean C2-band VOD (7.3 GHz; AMSR2); f) Mean X-band VOD (10.7 GHz; AMSR2). VOD is dimensionless and time-averaged for period April 2015-March 2016. Areas with insufficient VOD and/or ACD data (e.g. rivers edges and coastlines) are not plotted. Spatial scale: 25 km.

The VOD at C-bands (6.9 and 7.3 GHz, hereafter named C1 and C2, respectively) and X-band (10.7 GHz) are derived from the Advanced Microwave Scanning Radiometer 2 (AMSR2), on board the Japan Aerospace Exploration Agency's (JAXA) Global Change Observation Mission-1st Water (GCOM-W1) satellite. The ground resolutions of these bands are 35 x 62 km (C-band) and 24 x 42 km (X-band). VOD is retrieved with the Land Parameter Retrieval Model (LPRM; Owe et al., 2008), which uses an analytical relationship to predict VOD based on the Microwave Polarization Difference Index (MPDI; Meesters et al., 2005), emissivity and vegetation scattering albedo. The dataset is provided on a 25 km grid (Vrije Universiteit Amsterdam and NASA GSFC, 2014), and is adapted to the EASE 2.0 grid at the same scale using bilinear interpolation. The yearly averages are computed for each frequency band and are shown in Figures 1d, e and f.

#### *2.2.3. Enhanced Vegetation Index (EVI)*

The Enhanced Vegetation Index (EVI) is a VIS/NIR index used as a proxy of vegetation condition, photosynthetic activity, and biomass (Huete et al., 2002). Here it is used to provide comparison with the microwave datasets when their sensitivity to ACD and FC is studied. The EVI dataset is derived from MODIS. Original EVI data is the 16-day MODIS/Terra MOD13C1 v.6 product, on a 0.05° latitude/longitude global grid. EVI is converted to the EASE 2.0 grid at 25 km scale using bilinear interpolation.

#### *2.2.4. Forest cover maps*

The European Space Agency – Climate Change Initiative (ESA-CCI) 2015 Land Cover map (ESA-CCI, 2017; 300 m resolution) is used in this work to produce a binary forest mask and to obtain maps of forest cover percentages and flooded forest proportion. The land cover categories considered as forests in this research are tree covers as well as vegetation mosaics with (tree +

shrub) or (tree + shrub + herbaceous) covers occupying >50% of surface. Pixels at the study scales are classified as forests when this grouped category is dominant (modal class). Also, the forest cover (FC) variable is computed as the percentage of forests in the pixel and its contribution to the VOD is studied. Likewise, the proportion of flooded forests is also computed.

#### *2.2.5. Digital Elevation Model (DEM)*

To take into account the impact of increasing altitudes on ACD and VOD (mainly in the Andes) the ETOPO1 Global Relief Model (Amante and Eakins, 2009) is used. The ETOPO 1 provides global land elevation and ocean bathymetry at 1 arc-minute resolution. It is supplied by the National Oceanic and Atmospheric Administration (NOAA; NOAA, 2017). This dataset is aggregated at the studied spatial scale (25 km).

#### *2.2.6. Data screening*

Only pixels containing >95% of ACD high resolution information are considered, in order to guarantee a highly representative sample of the carbon dataset. Regions without VOD data are also excluded. The overall studied area is of ~1.3 million km<sup>2</sup>, containing ~900,000 km<sup>2</sup> of forests. More specific details are reported in Table S1.

### 2.3. Statistical methods

#### *2.3.1. Analysis of the VOD-ACD relationship*

VOD and ACD datasets are compared and their relationship is analysed for the entire study area. The spatial cross-correlation between VOD at each band and ACD is calculated and compared

using the Lee's Index, which is a bivariate spatial association method (Lee, 2001). This index is computed using the function 'lee' of the 'spdep' R package (Bivand et al., 2013; Bivand and Piras, 2015) at 25 km scale and for increasing distances from 25 km to 1,250 km. This computation allows capturing spatial association among observations in terms of their point-to-point relationships across the spatial patterns (Lee, 2001), and serves in this study to quantify and compare the sensitivity of each VOD band to spatial patterns of carbon density. Also, regressions of each VOD product as functions of ACD are estimated using Generalized Additive Models (GAM; Hastie and Tibshirani, 1990). GAMs have been previously used to explore the relationships between remote sensing data and biomass (Baccini et al., 2004) and forest structural attributes (Frescino et al., 2001). The 'gam' R package (Hastie, 2018) is used to compute these regressions using cubic spline smoothing classes.

The main focus of this work is on forests, which represent approximately 70% of the study region. Linear regressions of VOD as a function of ACD are computed for the entire forested area as:

$$VOD = a + b \cdot ACD \quad (1)$$

where *VOD* and *ACD* stand for vegetation optical depth at each band and above-ground carbon density, respectively, and *a* and *b* are constant terms. Linear functions have been chosen upon exploratory analyses of VOD-ACD scatter plots (see Section 3.1), and after discarding exponential and quadratic functions which did not improve the fitting (results not shown). In addition, Eq. (1) is specifically applied in the densest forests, where the penetration capacity of microwaves through vegetation could be reduced. Two categories of dense forests are studied:  $\geq 80$  TC/ha and  $\geq 100$  TC/ha.

Residuals for the L-band VOD – ACD regression in Eq. (1), computed as predicted minus observed VOD, are mapped to assess the impact of different geographical features on the VOD-ACD relationship in forests. The map of residuals is compared to maps of flooded forest

proportion and altitude. Also, the VOD-ACD residuals and the VOD values are plotted against altitude, flooded forest proportion, and ACD data.

Distinct VOD-ACD relationships are found at different altitudes, as well as in flooded forests, according to the analysis of residuals (see Section 3.1). For this reason, the analysis described in Eq. (1) is reproduced specifically for three different altitude groups (1,000 to 2,000 m; 2,000 to 3,000 m; and >3,000 m) and for two groups of flooded forest proportion (5 to 50%; and 50 to 100%). These categories are chosen due to their geographical location (mountain or flooded forest regions), their positive or negative residuals with respect to the VOD-ACD regression model in Eq. (1), and their differences in terms of carbon density. T-tests are used to check that these criteria are accomplished for the different groups. In particular, T-tests are applied to study whether the proposed categories presented residuals significantly different from 0, and to compare the proposed categories with the remaining regions (i.e., altitude <1,000 m and flooded forest <5%) in terms of ACD. These regions contained the vast majority of pixels and are considered as reference groups. Significance for t-tests is established at  $p < 0.05$ .

### *2.3.2. Relative contribution of carbon density and forest cover to VOD and EVI*

The spatial variability of VOD may be affected not only by ACD but also by spatial variations in forest cover (FC). Furthermore, both of these variables can change markedly through different altitudes, as altitude strongly conditions vegetation characteristics. In this case, the relationships are studied for VOD and for EVI (plotting both variables against ACD, FC and altitude), in order to compare the information provided by microwave and optical-infrared data.

To understand to what extent the VOD and EVI variability could depend on forest cover changes rather than on the inherent carbon density of forests, VOD and EVI datasets are studied as a function of ACD and FC using multiple regression:

$$VOD \text{ or } EVI = a + b \cdot ACD + c \cdot FC \quad (2)$$

where the response variables are *VOD* (i.e., the VOD at each band) or *EVI* (i.e., the Enhanced Vegetation Index), the explanatory variables are *ACD* and *FC*, which stand for above-ground carbon density and forest cover, respectively, and *a*, *b* and *c* are constant terms. Note that the equation terms will change for each band. This analysis is carried out in order to obtain the relative importance of ACD and FC on the VOD and EVI signals. The ‘lmg’ function of the ‘relaimpo’ R package (Grömping, 2006) has been used to this objective. This function provides the relative contribution of each variable in a linear regression (independently of correlations among the regressors) and is based on the averaging sequential sums of squares over all orderings of regressors (Lindeman et al., 1980, p. 119). This procedure is replicated for the altitude and flooded forest groups detailed in Section 2.3.1, in order to provide specific analysis in the Andes and in flooded regions, which have shown different patterns for the VOD-ACD relationship. Additionally, Eq. (2) is applied separately for different areas, providing a geographical division in six regions including Panama (A), Colombia and northern Peru (B), and four latitudinal strips in Peru: north-central Peru (C), central Peru (D), south-central Peru (E) and southern Peru (F). A map with this division is shown in Figure S1.

### **3. Results**

#### ***3.1. VOD-ACD relationship***

VOD and ACD maps are shown in Figure 1. The highest VOD and ACD values are found in the evergreen forests of Peru and Colombia, while both variables decrease in non-forested areas (especially in the Andes). At L-band, VOD is lower in the river edges and in flooded regions, partially reproducing reduced ACD in these areas. This qualitative pattern is less clear at C- and X-bands (Figure 1). L-band shows the highest spatial cross-correlation (Lee’s index) with ACD for

approximately 0 to 300 km distance. Both L- and C-bands show better spatial cross-correlation with ACD than X-band, independently of the distance analysed (Figure 2). Note that the decrease on the Lee's index with distance (Figure 2) might be also due to the uncertainty of ACD estimates, which is not accounted for here. This is further discussed in Section 4.1.

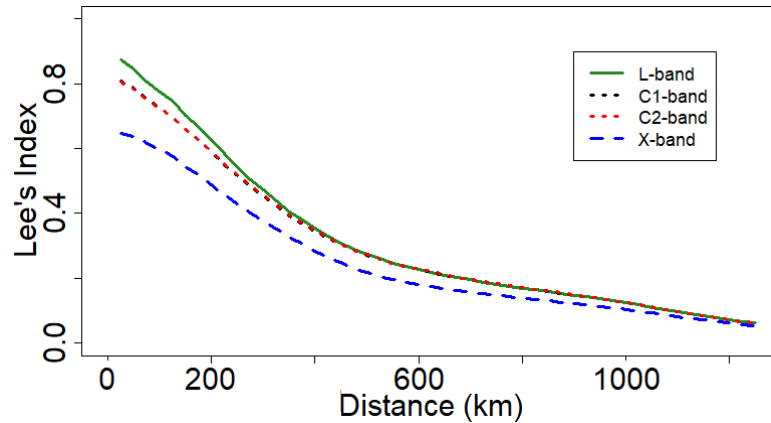


**Figure 2.** Spatial cross-correlation (Lee's Index) between ACD and each of the mean VOD datasets studied: L-band (green), C1-band (black), C2-band (red) and X-band (blue). Note that C1- and C2-bands are overlapped. Lee's Index is computed for each 25 km step to a maximum distance of 1,250 km.

Scatterplots in Figure 3 show the VOD-ACD relationships for the studied bands in the entire region. The sensitivity of VOD to ACD decreases according to the increasing frequencies studied (i.e., L-, C-, and X-band, respectively). In particular, results for GAM functions (Figure 3) show that the coefficients of determination ( $R^2$ ) are 0.83 for L-band, between 0.71 and 0.72 for C-bands, and 0.64 for X-band. Note that the term  $R^2$  must not be interpreted in this case as the VOD explained variance in the context of a linear regression. GAM curves change from a portion with very steep slopes (for  $ACD < 10$  TC/ha and  $VOD < 0.5$ , which correspond to non-forested regions) to gradually smoother slopes (for  $VOD > 0.5$  approximately, in forest areas). This change is continuous at L-band, but irregular at the other studied frequencies (Figure 3).



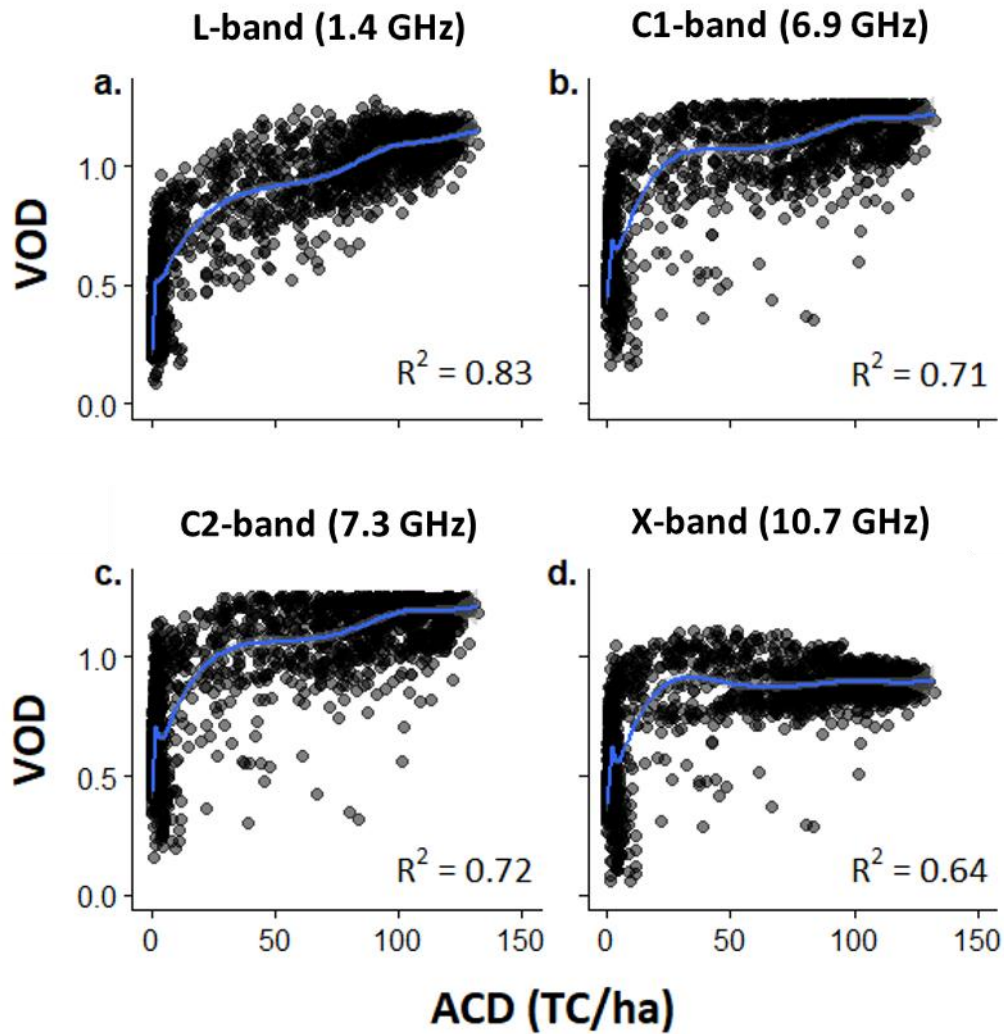


**Figure 3.** Regressions of VOD as a function of ACD using Generalized Additive Models (GAM). (a) L-band (1.4 GHz; SMAP); (b) C1-band (6.9 GHz; AMSR2); (c) C2-band (7.3 GHz; AMSR2); and (d) X-band (10.7 GHz; AMSR2). Models are fitted on the basis of a cubic spline function. Note that dark areas in the figure are due to a high density of points, while light grey represents isolated pixels in the regression. All regressions are significant ( $p < 0.0001$ ).

Linear regressions (Eq. 1) in forest areas are shown in Figure 4. The percentages of VOD variance explained by ACD are 57% (L-band), 30 to 32% (C-band), and 1% (X-band). Importantly, note that the shape of the VOD-ACD scatterplots suggests that the relationship between both variables in forests is not exactly linear (Figure 4). In that sense, it must be taken into account

that VOD shows decreased sensitivity to ACD changes in the densest forests (Table S2). Still, linear regression has shown similar or improved fitting in comparison to exponential and quadratic functions (see Section 2.3.1).

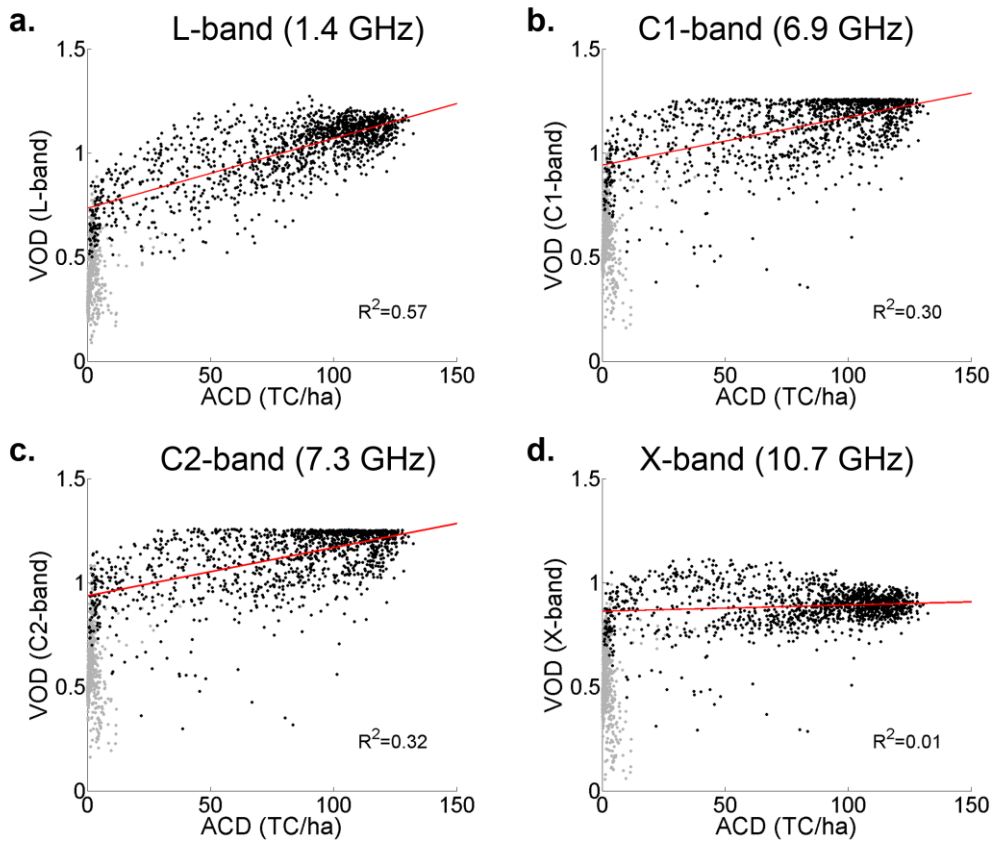


**Figure 4.** Linear regressions of VOD as a function of ACD (Eq. (1)) in forest areas. (a) L-band (1.4 GHz; SMAP); (b) C1-band (6.9 GHz; AMSR2); (c) C2-band (7.3 GHz; AMSR2); and (d) X-band (10.7 GHz; AMSR2). All regressions are significant ( $p<0.001$ ). Grey dots show pixels without forest dominant cover and are excluded from the regressions.

The analysis of residuals for the linear VOD-ACD relationship (Eq. 1) at L-band shows how positive residuals are associated with decreasing ACD and increasing altitudes in the Andes Mountains (Figures 5, S2a and S3). The sign of residuals changes above 3,000 m matching a

decrease on VOD values (Figures 5, S2a and b, and S3). Negative residuals of VOD at L-band are found in river edges and in flooded forest regions, where ACD and VOD are low for pixels with dominant flooded forest cover (Figures 5, S2c and d, and S3). Importantly, the relationship between the residuals and the fitted VOD values is shown in Figure S4. The observed patterns confirm that the VOD-ACD relationship is not completely linear. The geographical patterns for VOD residuals shown in Figure 6a might be also influenced by this fact.

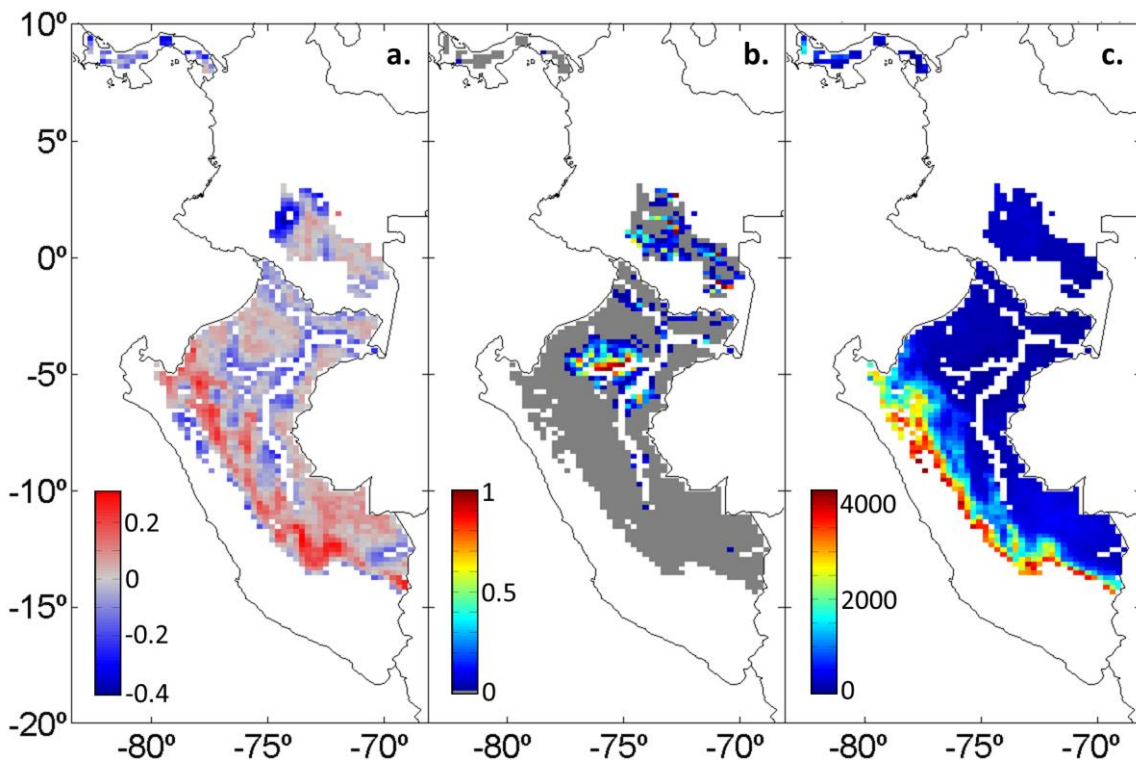


**Figure 5.** (a) Residuals for the L-band VOD-ACD regression (Eq. (1); note that residuals equal to 0 are plotted in grey color); (b) Percentage of flooded forest (grey=0%); (c) Altitude (m). Areas without dominant forest cover and areas with insufficient VOD and/or ACD data are not plotted.

Following the patterns described, T-tests for the different categories of altitude and flooded forest proportion (see Section 2.3.1) report that VOD residuals are significantly different from 0, and/or that ACD shows significant differences with reference groups, for all the studied

categories (Figure S3). This confirms that providing particular analyses for the proposed categories permits to study the VOD-ACD relationship in forests of different biomass, and in regions where the VOD, as a function of ACD, is overestimated or underestimated.

Figure 6 (a, b and c) shows regressions of L-band VOD as a function of ACD (Eq. (1)) at the three studied altitude ranges. It can be seen that the regression slopes increase with altitude, with  $R^2$  ranging from 0.51 to 0.61. Figure 6 (d and e) shows regressions (Eq. (1)) for flooded forest categories (5-50% cover:  $R^2 = 0.65$ ; 50-100% cover:  $R^2 = 0.72$ ).

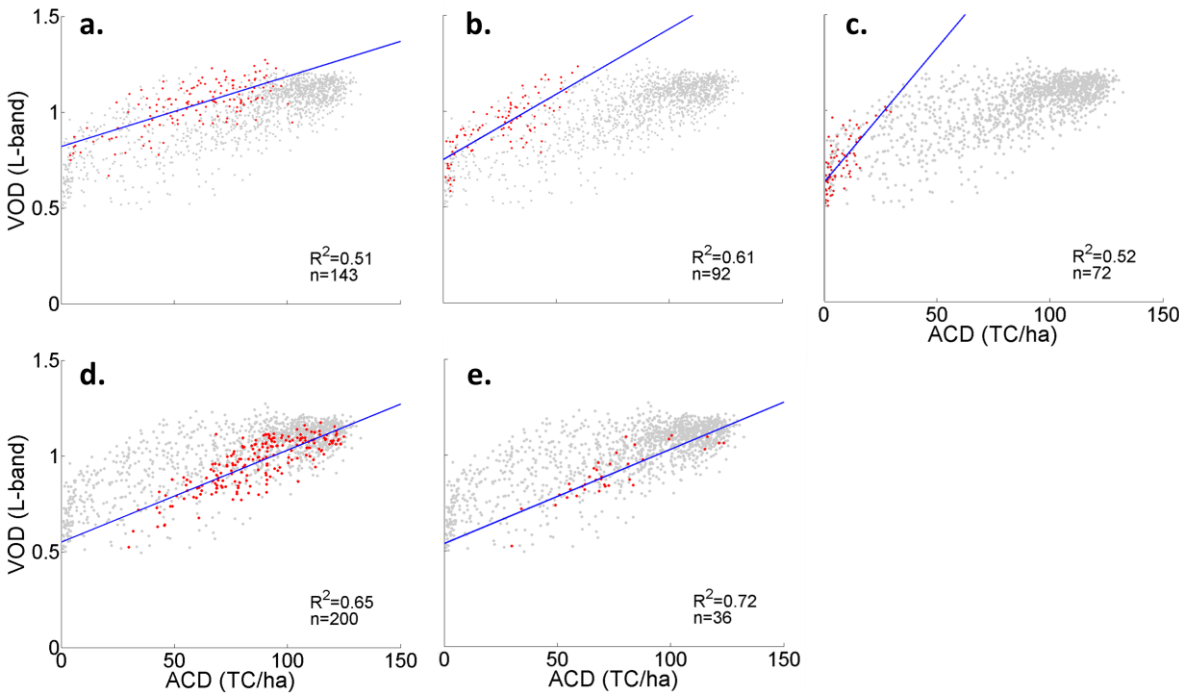


**Figure 6.** Regression of VOD as a function of ACD (Eq. (1); blue line) for different categories (red dots): (a) altitude (1,000 to 2,000 m); (b) altitude (2,000 to 3,000 m); (c) altitude (>3,000 m); (d) proportion of flooded forest (5 to 50%); (e) proportion of flooded forest (>50%). Grey dots represent the VOD-ACD data for all the forest pixels in the region.

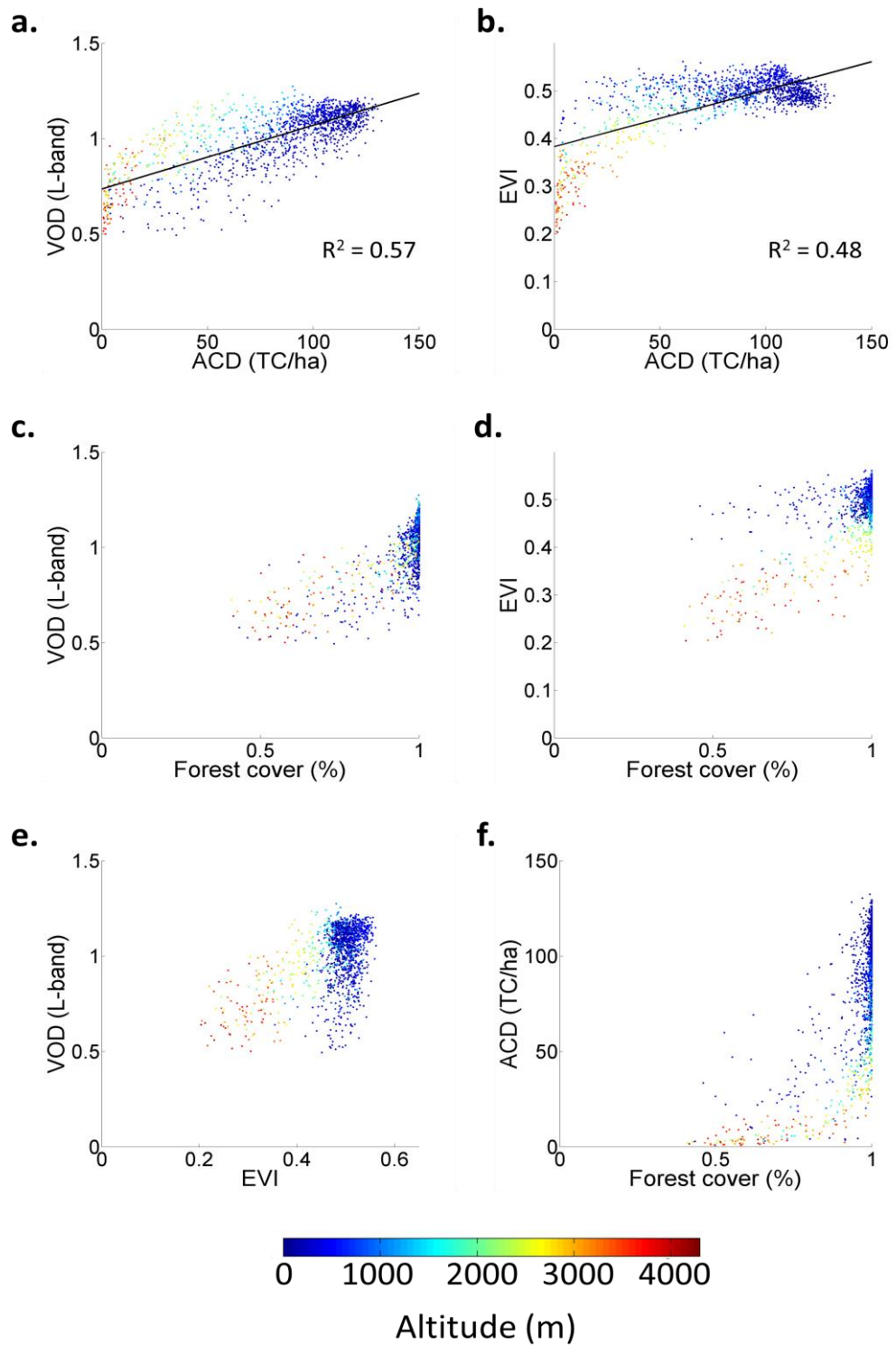
### 3.2. Contribution of carbon density and forest cover to VOD and EVI

Figure 7 shows the relationship of L-band VOD and EVI with ACD and FC, as well as the VOD-EVI and ACD-FC scatterplots. Note that the EVI is included here to provide comparison between microwave and visible-infrared datasets in forested areas. Altitude is shown as a third variable in each subplot. In Figures 7a and b it is reported that L-band VOD is more sensitive to ACD ( $R^2 = 0.57$ ) than EVI ( $R^2 = 0.48$ ). In turn, EVI is more sensitive to ACD than VOD at C- and X-bands (see Figure 7b, and compare it to Figure 4). Also, it is shown that VOD, EVI and ACD decrease for increasing altitudes. This effect is more evident for EVI than for VOD. Figure 7c shows VOD ranging from 0.5 to 1.25 in completely forested pixels, while its maximum decreases to 0.8 in pixels with less than 50% of forests. In the case of EVI, it is higher at low altitudes (especially <1,000 m), and its maximum also diminishes at low forest proportions. The latter pattern is clearer for higher altitudes, where EVI can drop below 0.2 (Figure 7d). Figure 7e shows a positive association between VOD and EVI in forests above 1,000 m. Note that ACD decreases with increasing altitude and decreasing forest cover proportion (Figure 7f).

The relative contribution of ACD and FC to the VOD and the EVI variances is provided in Figure 8. ACD explains 34.2% of L-band VOD variability, while this percentage decreases for EVI (26.9%), C-band (18% and 19.4% for C1 and C2, respectively), and X-band (negative coefficient). FC explains similar proportions of EVI (32.5%) and L-band VOD (30%). This proportion is lower at C- and X-bands (17.3% for C1, 15.9% for C2, and 9.1% for X-band). Overall, the relative contributions of ACD and FC are consistent for most of the studied regions, although the absolute percentages change (Figure S1). Additionally, in the southernmost region of Peru, EVI shows higher sensitivity to ACD and FC than any VOD band (Figure S1).

Figures 9a, b and c show how the ACD relative importance for L-band is higher than the ACD contribution to C- and X-bands and EVI in all cases. For L-band VOD, the ACD relative importance is similar regardless of the altitude group (30.6% to 34.4%). For VOD at C1- and X-

bands, the relative importance of ACD is higher above 2,000 m than at lower altitudes. In C2-band and EVI the ACD contribution is higher for the 2,000 – 3,000 m category. In Figures 9d and e the sensitivity of VOD to ACD in flooded regions is higher than the sensitivity found in the overall models shown in Figure 8, regardless of the frequency band. The relative contribution of ACD is higher than the relative contribution of FC in these regions. L-band VOD shows the highest sensitivity to ACD (relative importance from 51% to 62.8%), followed by C-bands (39.7% to 42.9%), and by X-band (29.3% to 32.6%), in this order. In contrast, ACD and FC show low and not significant contribution to EVI in flooded forests. EVI has a very low variability in these areas (from 0.45 to 0.49). This illustrates the added value of using microwave over optical remote sensing in flooded forests.



**Figure 7.** Relationships between: (a) ACD and L-band VOD (Eq. (1)), (b) ACD and EVI, (c) forest cover and L-band VOD, (d) forest cover and EVI, (e) EVI and L-band VOD, and (f) forest cover and ACD. In (a) and (b), linear regressions are significant ( $p < 0.0001$ ). Only forest pixels are plotted. Colour shows the altitude.

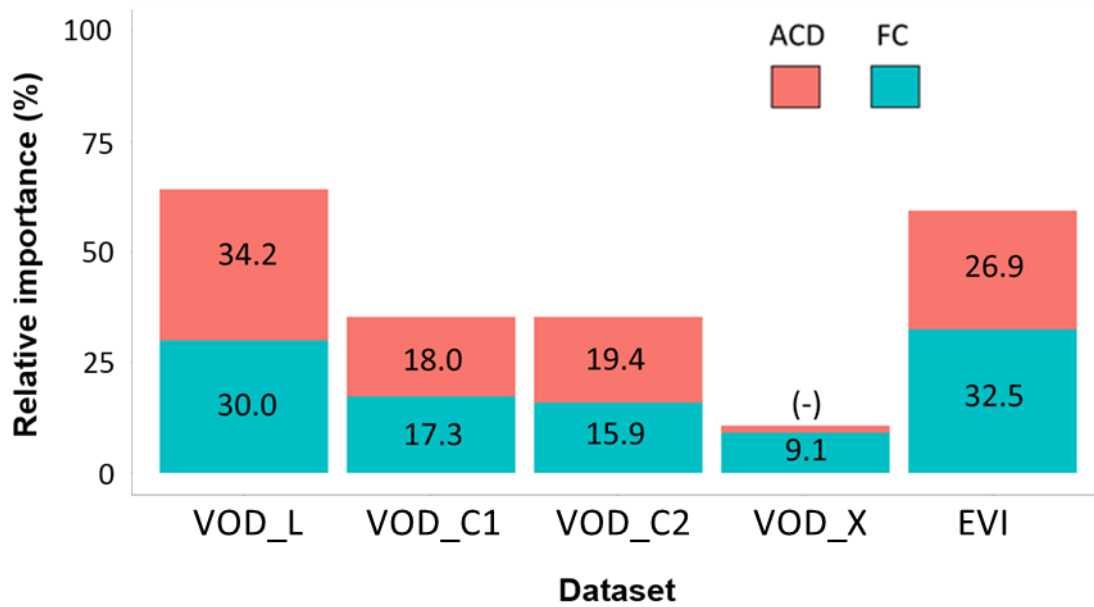


**Figure 8.** Relative importance of ACD and FC as predictors of VOD and EVI in Eq. (2). All effects are significant ( $p < 0.0001$ ). All effects are positive, except for the effect of ACD on X-band VOD which is negative (-). Numbers represent relative importance (%) of each variable. All results are significant ( $p < 0.0001$ ).



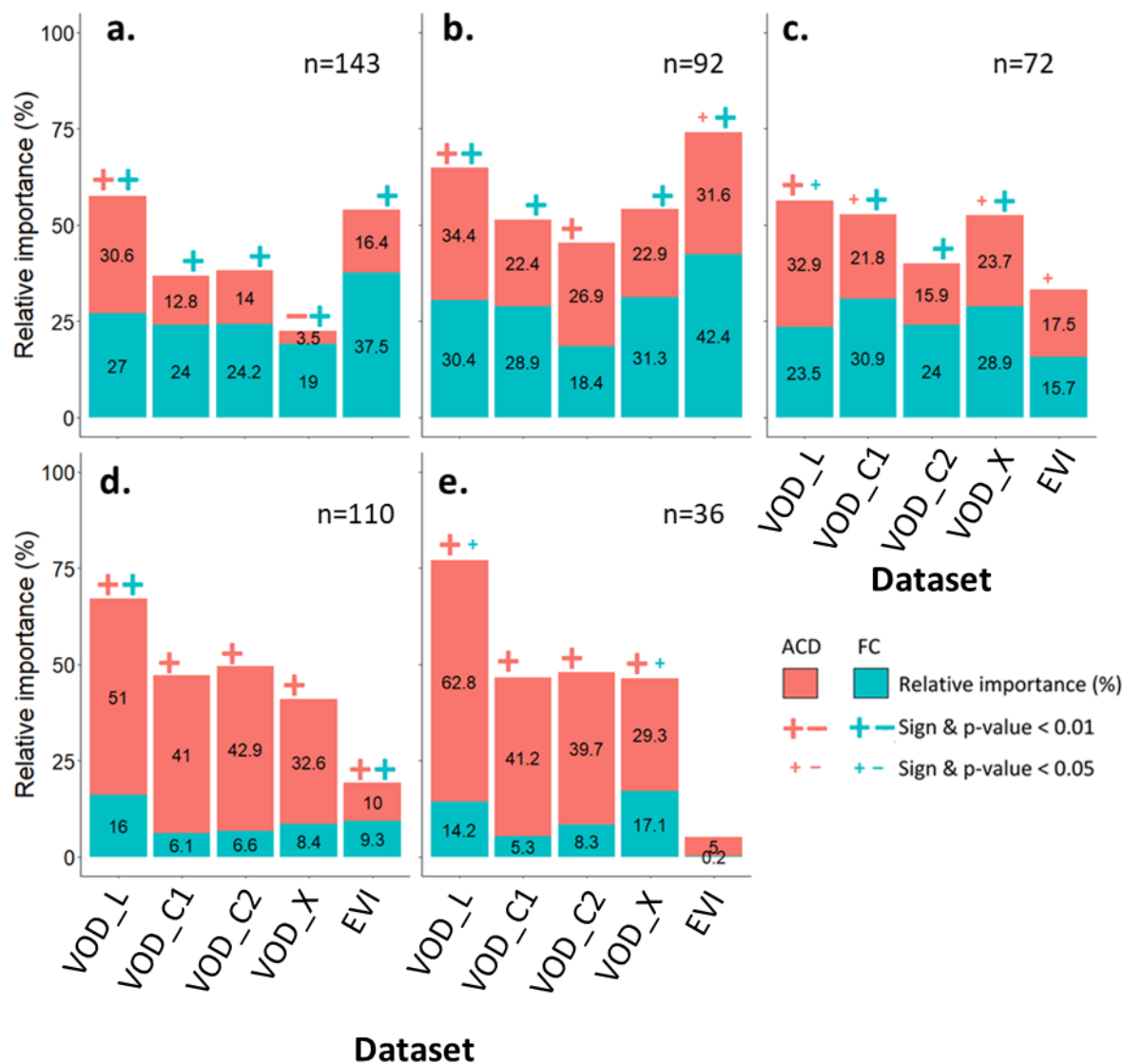


**Figure 9.** Relative importance of ACD and FC as predictors of VOD and EVI (Eq. (2)). Sign and significance for each variable are plotted if at least  $p < 0.05$ . If no sign is plotted, this means not significance at 95% confidence level (i.e.,  $p \geq 0.05$ ). Results in top row show altitudinal ranges: (a) 1000 to 2000 m; (b) 2000 to 3000 m; (c) >3000 m. Results in the bottom row show flooded forest categories: (d) 5 to 50%; (e) 50 to 100%. Letter n refers to the sample.

## **4. Discussion**

### **4.1. L-band VOD shows enhanced sensitivity to carbon stocks**

The ability of remote sensing techniques to capture vegetation carbon density largely depends on the sensitivity of the studied signal to biomass. The VOD-ACD relationship shows the existing link between wet, green and woody biomass in nature, as the ability of VOD to capture ACD depends on its sensitivity to the VWC and on its capacity of penetration through the canopy. Both characteristics should be a function of the microwave frequency used for the VOD retrieval. The results presented in this work confirm this fact, as VOD shows a greater sensitivity to ACD up to higher canopy densities with decreasing frequencies. Results are also consistent with the no saturation of L-band VOD at the highest carbon densities (as reported also in Brandt et al., 2018) in contrast to VOD from higher frequencies (Figures 3 and 4). According to theory, X-band VOD is only sensitive to the top of the canopy and displays the lowest values (see Figures 3 and 4). The greatest sensitivity of L-band in dense vegetation conditions stresses the advantage of using L-band VOD for mapping carbon stocks at local and regional scales (up to ~300 km; Figure 2). Additionally, note that the coarser ground resolution of the C-band channel might overestimate its spatial cross-correlation (comparatively to the other bands), suggesting that (i) L-band VOD applicability even at scales beyond 300 km could be advisable, and (ii) differences in Lee's index between C- and X-bands could be lower than those reported (in case that both products had similar ground resolutions).

GAM functions have captured the VOD-ACD patterns for both forest and non-forest regions, and the continuity on the L-band GAM curve in the transition zone suggests that this microwave frequency could be the most appropriate to capture biomass on vegetation transitions to forests (see Section 3.1 and Figure 3). The GAM functions fits (i) confirm the enhanced sensitivity of L-band VOD to ACD, (ii) show that the scarce frequency difference between C1 and C2 bands is not relevant to detect ACD changes, and (iii) confirm the lower

sensitivity of the X-band to carbon variability. Nevertheless, it should be noted that GAM functions are a statistical method more appropriate for exploratory analysis than for predictive purposes (Hastie and Tibshirani, 1990; Frescino et al., 2001; Baccini et al., 2004) and therefore other statistical tools would be preferable for predicting carbon stocks from satellite data.

In forest areas, results are also in agreement with the fact that the sensitivity of VOD to carbon density increases with decreasing microwave frequencies. Still, further work is needed to establish a more accurate VOD-ACD relationship in very dense forests. In that sense, (i) applying a mutual information analysis (Konings et al., 2015) would disentangle the VOD and ACD contributions and would provide a more robust estimate of their relationship; and (ii) complementarity among VOD bands, as well as among different datasets (e.g., EVI, LiDAR, or radar data) would increase the capacity to establish an accurate relationship (see Section 4.3). In addition, ACD estimates from VOD data would benefit from multi-year observations. In other studies this has allowed to provide estimates of carbon trends using VOD either at L-band (Brandt et al., 2018) or at C- and X-bands (Liu et al, 2015).

In the Andes Mountains, decreasing carbon density should be related to vegetation transitions through altitude. Positive residuals in this area (up to 3,000 m) can be explained by a different response to other vegetation types in the mountains and by uncertainties in the carbon density map (Asner et al., 2012). In contrast, negative residuals in regions above 3,000 m are consistent with low VOD values linked to complex topography (Konings, Piles, et al., 2017) and to low carbon density. Modelling carbon stocks in the Andean forests would need calibration considering different elevation (or different vegetation types linked to elevation), as slopes for the VOD-ACD regression increase with decreasing ACD at different heights (Figures 6a, b and c).

Concerning flooded forests and river edges, these regions can be flooded up to ten months a year (WWF, 2018). The presence of standing water in vegetation drastically reduces VOD and thus could explain the negative residuals observed in the VOD-ACD relationship in these

regions. This effect has been previously observed in C-band VOD over flood plains of large rivers (e.g., the Zambezi, the Mekong or the Ganges; Jones et al., 2011) and in L-band VOD over rice fields in Thailand (Piles et al., 2017). In these cases, VOD decreased while vegetation grew in inundated regions. It is suggested that VOD dampens under flood conditions because (i) a higher dielectric constant of standing water leads to lower emissivity on horizontal polarization ( $e_h$ ), (ii) vegetation such as grasses or reeds (i.e., vertically oriented), which may emerge in flooded areas, might maintain the emissivity in vertical polarization ( $e_v$ ; which would be expected to decrease in flooded conditions), and (iii) the fact that water masks the soil emissions (Jones et al., 2011; Piles et al., 2017). Finally, note that the slope for the VOD-ACD regression in flooded regions is similar for the two categories of flooded forest proportion (Figures 6d and e), suggesting that a single relationship can be derived in this forest type.

Additionally, it should be stressed that vegetation mosaics (southern Panama and northern of the Colombian study region) show negative residuals because the VOD-ACD regression is dominated by evergreen forests. These present larger ACD and VOD values if compared to those from vegetation mosaics. Further work is needed to provide specific analyses in these regions.

Finally, note that the VOD residuals may respond partially to other factors which should also be mentioned. Firstly, the distribution of the residuals values shows that the VOD-ACD relationship is not completely linear (Figure S4). This may lead to overestimations and underestimations of VOD. Nevertheless, other fitting functions studied did not report different results (see Section 2.3.1; results not shown). Secondly, note that the sources of VOD data contain inherent variability which depends on the sensors (i.e. SMAP/AMRS2), on the algorithm used (i.e. MT-DCA/LPRM) and on the version of these algorithms (e.g., different versions of the LPRM are available). This might also partially contribute to the variability on the VOD-ACD relationship. Thirdly, the uncertainty of ACD estimates may be a source of spatial variability

which must be considered to calibrate carbon stock models. The main sources of uncertainty are (i) the validity of the relationship between the LiDAR tree height measures and the ACD values, (ii) the extrapolation of LiDAR ACD estimates to regional scales (Asner et al., 2012), and (iii) the fact that ACD and VOD datasets have been acquired in different time periods. Concerning to the latter, recent research shows steady carbon trends in most of the region, or small changes (<10% of the total ACD values) in some specific regions of Peru and Colombia (see Figure 3 in Liu et al., 2015). Hence, the effect of these differences is probably limited to an additional source of spatial variability with low impact in the VOD-ACD relationships in terms of comparison among the different frequencies.

#### **4.2. Carbon density and forest cover contributions to VOD and EVI**

VOD changes can be explained by a combined effect of carbon stocks and forest cover (the latter limits the variability of VOD and ACD; Figure 7). Interestingly, the VOD variance explained by ACD in Eq. (2) is also decreasing with increasing microwave frequencies (Figure 8). This is consistent with the discussion provided in Section 4.1. Furthermore, ACD and FC show similar contribution to the VOD variability at the studied bands (Figure 8), and the addition of the FC variable (see Eq. (2)) to the VOD-ACD regression shown in Eq. (1) does not result in an important increase of the explained VOD variance (only between 3% and 8% depending on the VOD frequency). Consequently, approximately half of the VOD variance initially explained by ACD (see Section 3.1) is due to the spatial variability in forest cover. Nevertheless, the relative importance of the ACD and FC variables changes among regions (Section 3.2), possibly due to different variability of ACD or to different vegetation patterns (e.g., evergreen forest in Peru contrasts with vegetation mosaics in Panama; Figure 1a).

To explore the complementarity and differences between VOD and VIS/NIR indices, MODIS-derived EVI has been included in the study. L-band is the only VOD dataset showing

greater sensitivity to ACD than EVI. Nevertheless, forest cover has greater relative importance than ACD on the EVI signal, which is coherent to the low canopy penetration of VIS/NIR indices. In addition, it should be noted that (i) EVI shows no association with L-band VOD in forests below 1,000 m, and (ii) EVI equals or enhances the sensitivity to ACD in regions D and F with respect to L-band VOD (see Section 3.2). In general, the results presented are in agreement with other studies reporting that -at the global scale- L-band VOD shows lower correlation with VIS/NIR indices than VOD at higher frequencies. This is consistent with the deeper penetration capacity of L-band microwaves, and suggests that L-band VOD and optical indices can complement each other because they provide information from different layers within the vegetation canopy (Jones et al., 2011; Grant et al., 2016).

Results show that the higher sensitivity of L-band VOD to ACD is consistent and similar across different altitude classes (i.e., among groups with different ACD; Figures 9 and S3). In the studied altitude groups, the joint ACD + FC contribution to the VOD at C- and X-bands and to the EVI signal is higher than the observed in the entire study area (Figure 9). This effect is not consistently increasing with altitude, nor significant in some cases, but in general it is consistent to the fact that higher VOD frequencies and EVI have a greater sensitivity to changes in canopy and biomass in less dense forests. Dividing altitude into three separate groups enables a more detailed analysis, but it also limits the ranges of the studied variables and thus reduces their resulting relative importance. This can explain why only the 2,000 – 3,000 m category reports a high weight of ACD on EVI (Figure 9b), when positive EVI-ACD and EVI-VOD trends are found above 1,000 m (Figures 7b and 7e). These trends are in agreement with the results in Todd et al. (1998), which show that NDVI can be considered an accurate proxy of biomass in areas of low vegetation density.

Consistently with previous results, in flooded forests the VOD at L-band shows higher sensitivity to ACD than the VOD at higher frequencies. Interestingly, ACD in flooded forests

explains an important proportion of VOD also at C- and X-bands (Figures 9d and e). Flooded forests are complex ecosystems which include several vegetation stages (grasses, shrubs, and early and late successional forests; Daly and Mitchell, 2000; WWF, 2018). This causes a complex structure in terms of vegetation distribution, height, and biomass, as well as lower ACD, which can explain the better response of VOD to carbon. In contrast, EVI has reached saturation and therefore shows very low variability in this area, and forest cover contribution to the studied variables is marginal, as the forest proportion is high and homogenous (95% of flooded forest pixels present >90% of forest proportion). Hence, VOD could potentially contribute to the study of carbon balance in flooded forests, which remains poorly known and hard to investigate with classical spectral indexes (Davidson et al., 2012). This analysis should be extended to river edges of the Amazon and its tributaries, which are flooded seasonally (and present accordingly negative residuals). Nevertheless, it must be noted that the moderate uncertainty of the ACD dataset in these regions (see Section 2.2.1) would difficult the calibration of VOD-ACD models, thus diminishing the accuracy of carbon estimates from satellite sources in these areas.

#### **4.3. Synergy of L-band VOD with multiple remote sensing sources to enhance carbon estimates**

The SMAP-derived L-band VOD information is sensitive to carbon density through most of the study area, and could improve the capacity of EVI and VOD at higher frequencies to estimate carbon stocks. Nevertheless, the sensitivity of VOD is decreased at high vegetation densities ( $\geq 80$  TC/ha). This represents approximately 60% of forests in the studied region. In this regard, future missions operating at lower frequency bands and therefore with greater penetration capacity through vegetation would probably be beneficial complementing current VOD estimates. This is the case of the BIOMASS mission (expected in 2020), specifically designed to measure forests and their biomass with a P-band (435 MHz) synthetic aperture radar. The combined use of L- and

P-band sensors should provide improved assessments of carbon density in very dense vegetation.

Remote sensing sources can be blended for more accurate carbon estimates, as the synergy among different remote sensing techniques can overcome the limitations from each data source (Goetz et al., 2009). In this study, it has been shown how EVI information could complement L-band VOD, especially in southern Peru and in montane forests. The L-band VOD-EVI joint application for mapping carbon stocks should be a matter of future work. The synergetic use of VOD at different frequencies (at least L-, C- and X-bands) and EVI would be particularly appropriate for biomass studies in vegetation transitions of the tropical montane forests. In the case of flooded forests, VOD data at different bands could have great potential for biomass estimation when used in a synergistic fashion. In this forest type, the combined application of VOD and LiDAR should also be investigated, as flooded forests are complex in terms of vegetation height variability, and LiDAR presents the unique capacity of capturing the vertical structure of vegetation. In that sense, the upcoming GEDI mission is expected to provide high resolution information of the forest canopy. Additionally, EVI has shown limited sensitivity to carbon changes in flooded forests, and SAR leads to biomass overestimation in flooded areas (Lucas et al., 2015).

It is worth saying that recent research has provided carbon trend estimates at continental and global scales using VOD data at L-band (Brandt et al., 2018) and at C- and X-bands (Liu et al., 2015). Importantly, the application of C- and X-bands VOD, LiDAR, and VIS/NIR indices, has led to new global biomass datasets (Liu et al., 2011; Saatchi et al., 2011; Avitabile et al., 2016; Baccini et al., 2017). Hence, the synergy between L-band VOD and other remote sensing sources can contribute to enhance carbon mapping and reduce its uncertainties.



## 5. Conclusions

This research provides a comparison of SMAP-derived L-band VOD with other VOD products from higher frequencies (from AMSR2 C- and X-bands) and with MODIS-EVI, in terms of their sensitivity to vegetation carbon stocks in Peru, Panama and southern Colombia. To this purpose, the remote sensing variables have been analysed as a function of Above-ground Carbon Density (ACD) data obtained by airborne LiDAR. L-band VOD has a higher sensitivity to carbon up to higher densities, and this sensitivity decreases in order with C- and X-bands, consistently with their increasing frequencies. Therefore, results confirm a fundamental physical phenomenon: lower frequency bands allow capturing the attenuation of soil emissivity due to vegetation as it passes through the whole vegetation canopy. A spatial cross-correlation analysis has shown that the capacity to reproduce carbon spatial patterns at local and regional scales decreases following increasing frequencies. Generalized Additive Models (GAM) and linear regressions of VOD as a function of ACD have confirmed the enhanced sensitivity of L-band VOD to carbon variability. The combined effect of the ACD and the forest cover proportion (FC) on the VOD and the EVI signals has been disentangled and quantified analysing the relative importance of each variable in bilinear regressions. At L-band, ACD and FC explain 34% and 30% of VOD variance in tropical forests of the region, respectively.

The study has been stratified by altitude and regions, and a particular analysis has been conducted in flooded forests. Results confirm that L-band VOD presents the strongest relationship to ACD regardless of altitude, vegetation covers and carbon density. These results are also consistent through the studied regions, except in southern Peru, where EVI shows higher sensitivity to ACD than L-band VOD. Also, it has to be noted that (i) ACD and FC partially represent an important contribution to EVI and VOD at C- and X-bands when lower density forests are studied in the Andes, (ii) VOD at all bands shows significant, positive, and strong relationship with ACD and FC in flooded forests, and (iii) an important proportion of evergreen forests in the region (those with the highest carbon densities) should be further analysed to

establish a more accurate VOD-ACD relationship. Hence, it is suggested that the complementary use of L-band VOD with VOD at other frequencies and with different remote sensing sources would be needed. In particular, (i) the future BIOMASS mission, with a P-band SAR on board (Le Toan et al., 2011; ESA, 2018), would have higher penetration to canopy layers and therefore would improve or complement the present VOD estimates on dense evergreen forests; (ii) the combined application of L-band VOD and the future GEDI LiDAR measurements could provide accurate ACD estimates in flooded forests; and (iii) the synergetic application of VIS/NIR indices and L-band VOD could enhance biomass estimates in forests with lower carbon density, such as montane ones. This study presents evidence that L-band VOD is a promising ecological indicator that could help enhancing present global biomass estimates, thus providing a new step forward on understanding the Earth carbon budget.

## **6. Acknowledgements**

The L-band VOD data are available from the authors upon request. This study has been supported by the Spanish government through the projects ESP2015-67549-C3-1-R and ESP2017-89463-C3-2-R, through the pre-doctoral grant “Ayudas para contratos predoctorales para la Formación de Doctores”, with reference BES-2013-066240, and through the award “Unidad de Excelencia Maria de Maeztu” MDM-2016-0600, financed by the “Agencia Estatal de Investigación” (Spain). The study has been supported also by the European Regional development Fund (ERDF). Maria Piles is supported by a Ramón y Cajal contract (MINECO). We thank the Carnegie Airborne Observatory for making the AGB maps available.

## **7. References**

684 Al Bitar, A., Mialon, A., Kerr, Y. H., Cabot, F., Richaume, P., Jacquette, E., ... & Al-Yaari, A. (2017).  
685 The global SMOS Level 3 daily soil moisture and brightness temperature maps. *Earth System*  
686 *Science Data*, 9(1), 293. doi: 10.5194/essd-9-293-2017, 2017.

687 Amante, C., & Eakins, B.W. (2009). ETOPO1 1 Arc-Minute Global Relief Model: Procedures, Data  
688 Sources and Analysis. NOAA Technical Memorandum NESDIS NGDC-24. National Geophysical  
689 Data Center, NOAA. [Last accessed 20th February 2018]. doi:10.7289/V5C8276M

690 Asner, G. P., Clark, J. K., Mascaro, J., García, G. G., Chadwick, K. D., Encinales, D. N., ... & Balaji, A.  
691 (2012). High-resolution mapping of forest carbon stocks in the Colombian Amazon.  
692 *Biogeosciences*, 9(7), 2683. doi:10.5194/bg-9-2683-2012.

693 Asner, G. P., Mascaro, J., Anderson, C., Knapp, D. E., Martin, R. E., Kennedy-Bowdoin, T., ... &  
694 Potvin, C. (2013). High-fidelity national carbon mapping for resource management and REDD+.  
695 *Carbon Balance and Management*, 8(1), 7. doi: 10.1186/1750-0680-8-7.

696 Asner, G. P., Knapp, D. E., Martin, R. E., Tupayachi, R., Anderson, C. B., Mascaro, J., ... & Llactayo,  
697 W. (2014). Targeted carbon conservation at national scales with high-resolution monitoring.  
698 *Proceedings of the National Academy of Sciences*, 111(47), E5016-E5022. doi:  
699 10.1073/pnas.1419550111.

700 Avitabile, V., Herold, M., Heuvelink, G. B. M., Lewis, S. L., Phillips, O. L., Asner, G. P., ... & Willcock,  
701 S. (2016). An integrated pan-tropical biomass map using multiple reference datasets. *Global*  
702 *Change Biology*, 22(4), 1406–1420. doi:10.1111/gcb.13139.

703 Baccini, A., Friedl, M. A., Woodcock, C. E., & Warbington, R. (2004). Forest biomass estimation  
704 over regional scales using multisource data. *Geophysical Research Letters*, 31(10). doi:  
705 10.1029/2004GL019782.

706 Baccini, A., Laporte, N., Goetz, S. J., Sun, M., & Dong, H. (2008). A first map of tropical Africa's  
 707 above-ground biomass derived from satellite imagery. *Environmental Research Letters*, 3(4),  
 708 045011. doi:10.1088/1748-9326/3/4/045011.

709 Baccini, A. G. S. J., Goetz, S. J., Walker, W. S., Laporte, N. T., Sun, M., Sulla-Menashe, D., ... &  
 710 Samanta, S. (2012). Estimated carbon dioxide emissions from tropical deforestation improved by  
 711 carbon-density maps. *Nature Climate Change*, 2(3), 182. doi: 10.1038/nclimate1354.

712 Baccini, A., Walker, W., Carvalho, L., Farina, M., Sulla-Menashe, D., & Houghton, R. A. (2017).  
 713 Tropical forests are a net carbon source based on aboveground measurements of gain and loss.  
 714 *Science*, 358(6360), 230-234. doi: 10.1126/science.aam5962.

715 Bivand, R., Hauke, J., & Kossowski, T. (2013). Computing the Jacobian in Gaussian spatial  
 716 autoregressive models: an illustrated comparison of available methods. *Geographical Analysis*,  
 717 45(2), 150-179. doi: 10.1111/gean.12008.

718 Bivand, R., & Piras, G. (2015). Comparing implementations of estimation methods for spatial  
 719 econometrics. *Journal of Statistical Software*, 63(18). doi: 10.18637/jss.v063.i18.

720 Blackard, J. A., Finco, M. V., Helmer, E. H., Holden, G. R., Hoppus, M. L., Jacobs, D. M., ... & Tymcio,  
 721 R.P. (2008). Mapping US forest biomass using nationwide forest inventory data and moderate  
 722 resolution information. *Remote Sensing of Environment*, 112(4), 1658-1677. doi:  
 723 10.1016/j.rse.2007.08.021.

724 Bouvet, A., Mermoz, S., Le Toan, T., Villard, L., Mathieu, R., Naidoo, L., & Asner, G. P. (2018). An  
 725 above-ground biomass map of African savannahs and woodlands at 25m resolution derived from  
 726 ALOS PALSAR. *Remote Sensing of Environment*, 206, 156-173. doi: 10.1016/j.rse.2017.12.030.

727 Brandt, M., Rasmussen, K., Peñuelas, J., Tian, F., Schurgers, G., Verger, A., ... & Fensholt, R. (2017).  
 728 Human population growth offsets climate-driven increase in woody vegetation in sub-Saharan  
 729 Africa. *Nature Ecology & Evolution*, 1(4), 0081. doi: 10.1038/s41559-017-0081

730 Brandt, M., Wigneron, J. P., Chave, J., Tagesson, T., Penuelas, J., Ciais, P., ... & Rodriguez-  
 731 Fernandez, N. (2018). Satellite passive microwaves reveal recent climate-induced carbon losses  
 732 in African drylands. *Nature Ecology & Evolution*, 2, 827-835. doi: 10.1038/s41559-018-0530-6.

733 Chaparro, D., Piles, M., Vall-llossera, M., Camps, A., Konings, A.G., Entekhabi, D. (2018). L-band  
 734 vegetation optical depth seasonal metrics for crop yield assessment. *Remote Sensing of*  
 735 *Environment*, 212C, 249-259.

736 Chaubell, J. (2016). Algorithm theoretical basis document. SMAP L1B enhancement radiometer  
 737 brightness temperature data product. Jet Propulsion Laboratory, California Institute of  
 738 Technology.

739 Daly, D. C. & J. D. Mitchell. (2000). Lowland vegetation of tropical South America – an overview.  
 740 Pages 391-454. In: D. Lentz, ed. Imperfect Balance: Landscape Transformations in the pre-  
 741 Colombian Americas. Colombia University Press, New York.

742 Davidson, E. A., de Araújo, A. C., Artaxo, P., Balch, J. K., Brown, I. F., Bustamante, M. M., ... &  
 743 Munger, J. W. (2012). The Amazon basin in transition. *Nature*, 481(7381), 321.  
 744 doi:10.1038/nature10717.

745 Dong, J., Kaufmann, R. K., Myneni, R. B., Tucker, C. J., Kauppi, P. E., Liski, J., ... & Hughes, M. K.  
 746 (2003). Remote sensing estimates of boreal and temperate forest woody biomass: carbon pools,  
 747 sources, and sinks. *Remote Sensing of Environment*, 84(3), 393-410.

748 Entekhabi, D., Njoku, E. G., O'Neill, P. E., Kellogg, K. H., Crow, W. T., Edelstein, W. N., ... & Kimball,  
 749 J. (2010). The Soil Moisture Active Passive (SMAP) mission. *Proceedings of the IEEE*, 98(5), 704-  
 750 716. doi: 10.1109/JPROC.2010.2043918.

751 ESA. European Space Agency. (2018). Future missions. BIOMASS. Retrieved from:  
 752 [https://m.esa.int/Our\\_Activities/Observing\\_the\\_Earth/The\\_Living\\_Planet\\_Programme/Earth\\_E](https://m.esa.int/Our_Activities/Observing_the_Earth/The_Living_Planet_Programme/Earth_E)  
 753 [xplorers/Future\\_missions/Biomass](https://m.esa.int/Our_Activities/Observing_the_Earth/The_Living_Planet_Programme/Earth_E)

754 ESA-CCI. European Space Agency – Climate Change Initiative. (2017). The European Space  
 755 Agency – Climate Change Initiative (ESA-CCI) 2015 Land Cover map. Retrieved from:  
 756 <https://www.esa-landcover-cci.org>.

757 European Commission. (2017). Global surface water explorer. Retrieved from: [https://global-](https://global-surface-water.appspot.com)  
 758 [surface-water.appspot.com](https://global-surface-water.appspot.com).

759 Fernandez-Moran, R., Al-Yaari, A., Mialon, A., Mahmoodi, A., Al Bitar, A., De Lannoy, G., ... &  
 760 Wigneron, J. P. (2017). SMOS-IC: An alternative SMOS soil moisture and vegetation optical depth  
 761 product. *Remote Sensing*, 9(5), 457. doi: 10.3390/rs9050457.

762 Frescino, T. S., Edwards, T. C., & Moisen, G. G. (2001). Modeling spatially explicit forest structural  
 763 attributes using generalized additive models. *Journal of Vegetation Science*, 12(1), 15-26. doi:  
 764 10.1111/j.1654-1103.2001.tb02613.x.

765 Goetz, S. J., Baccini, A., Laporte, N. T., Johns, T., Walker, W., Kelldorfer, J., ... & Sun, M. (2009).  
 766 Mapping and monitoring carbon stocks with satellite observations: a comparison of methods.  
 767 *Carbon Balance and Management*, 4(1), 2. doi:10.1186/1750-0680-4-2.

768 González-Alonso, F., Merino-De-Miguel, S., Roldán-Zamarrón, A., García-Gigorro, S., & Cuevas, J.  
 769 M. (2006). Forest biomass estimation through NDVI composites. The role of remotely sensed  
 770 data to assess Spanish forests as carbon sinks. *International Journal of Remote Sensing*, 27(24),  
 771 5409-5415. doi: 10.1080/01431160600830748.

772 González-Gambau, V., Olmedo, E., Turiel, A., Martínez, J., Ballabrera-Poy, J., Portabella, M., &  
 773 Piles, M. (2016). Enhancing SMOS brightness temperatures over the ocean using the nodal  
 774 sampling image reconstruction technique. *Remote Sensing of Environment*, 180, 205-220. doi:  
 775 10.1016/j.rse.2015.12.032.

776 Grant, J. P., Wigneron, J. P., De Jeu, R. A. M., Lawrence, H., Mialon, A., Richaume, P., ... & Kerr, Y.  
 777 (2016). Comparison of SMOS and AMSR-E vegetation optical depth to four MODIS-based

778 vegetation indices. *Remote Sensing of Environment*, 172, 87-100. doi:  
779 10.1016/j.rse.2015.10.021.

780 Grömping, U. (2006). Relative importance for linear regression in R: the package relaimpo.  
781 *Journal of Statistical Software*, 17(1), 1-27.

782 Hamdan, O., Aziz, H. K., & Rahman, K. A. (2011). Remotely sensed L-Band SAR data for tropical  
783 forest biomass estimation. *Journal of Tropical Forest Science*, 23(3), 318-327.

784 Hastie, T. J., and Tibshirani, R.J. (1990). Generalized Additive Models. Chapman and Hall, New  
785 York.

786 Hastie, T. (2018). GAM: Generalized Additive Models. R package version 1.15. Retrieved from:  
787 <https://CRAN.R-project.org/package=gam>

788 Huete, A., Didan, K., Miura, T., Rodriguez, E. P., Gao, X., & Ferreira, L. G. (2002). Overview of the  
789 radiometric and biophysical performance of the MODIS vegetation indices. *Remote Sensing of*  
790 *Environment*, 83(1-2), 195-213. doi: 10.1016/S0034-4257(02)00096-2.

791 Jackson, T. J., & Schmugge, T. J. (1991). Vegetation effects on the microwave emission of soils.  
792 *Remote Sensing of Environment*, 36(3), 203-212. doi: 10.1016/0034-4257(91)90057-D.

793 Jones, M. O., Jones, L. A., Kimball, J. S., & McDonald, K. C. (2011). Satellite passive microwave  
794 remote sensing for monitoring global land surface phenology. *Remote Sensing of Environment*,  
795 115(4), 1102-1114. doi: 10.1016/j.rse.2010.12.015.

796 Kerr, Y. H., Waldteufel, P., Wigneron, J. P., Delwart, S., Cabot, F., Boutin, J., ... & Juglea, S. E. (2010).  
797 The SMOS mission: new tool for monitoring key elements of the global water cycle. *Proceedings*  
798 *of the IEEE*, 98(5), 666-687. doi: 10.1109/JPROC.2010.2043032.

799 Konings, A. G., McColl, K. A., Piles, M., & Entekhabi, D. (2015). How many parameters can be  
800 maximally estimated from a set of measurements? *IEEE Geoscience and Remote Sensing Letters*,  
801 12(5), 1081-1085. doi: 10.1109/LGRS.2014.2381641.

802 Konings, A. G., Piles, M., Rötzer, K., McColl, K. A., Chan, S. K., & Entekhabi, D. (2016). Vegetation  
803 optical depth and scattering albedo retrieval using time series of dual-polarized L-band  
804 radiometer observations. *Remote Sensing of Environment*, 172, 178-189. doi:  
805 10.1016/j.rse.2015.11.009.

806 Konings, A. G., Piles, M., Das, N., & Entekhabi, D. (2017). L-band vegetation optical depth and  
807 effective scattering albedo estimation from SMAP. *Remote Sensing of Environment*, 198, 460-  
808 470. doi: 10.1016/j.rse.2017.06.037.

809 Kuplich, T. M., Salvatori, V., & Curran, P. J. (2000). JERS-1/SAR backscatter and its relationship  
810 with biomass of regenerating forests. *International Journal of Remote Sensing*, 21(12), 2513-  
811 2518. doi: 10.1080/01431160050030600.

812 Le Quéré, C., Raupach, M. R., Canadell, J. G., Marland, G., Bopp, L., Ciais, P., ... & Friedlingstein,  
813 P. (2009). Trends in the sources and sinks of carbon dioxide. *Nature Geoscience*, 2(12), 831. doi:  
814 10.1038/ngeo689.

815 Le Quéré, C. L., Andrew, R. M., Canadell, J. G., Sitch, S., Korsbakken, J. I., Peters, G. P., ... & Keeling,  
816 R. F. (2016). Global carbon budget 2016. *Earth System Science Data*, 8(2), 605-649. doi:  
817 10.5194/essd-8-605-2016.

818 Le Toan, T., Quegan, S., Davidson, M. W. J., Balzter, H., Paillou, P., Papathanassiou, K., ... & Ulander,  
819 L. (2011). The BIOMASS mission: Mapping global forest biomass to better understand the  
820 terrestrial carbon cycle. *Remote Sensing of Environment*, 115(11), 2850-2860. doi:  
821 10.1016/j.rse.2011.03.020.



822 Lee, S. I. (2001). Developing a bivariate spatial association measure: an integration of Pearson's  
823 r and Moran's I. *Journal of Geographical Systems*, 3(4), 369-385. doi: 10.1007/s101090100064.

824 Lindeman, R.H., Merenda, P.F., Gold, R.Z. (1980). Introduction to Bivariate and Multivariate  
825 Analysis. Scott, Foresman, Glenview, IL.

826 Liu, Y. Y., de Jeu, R. A., McCabe, M. F., Evans, J. P., & van Dijk, A. I. (2011). Global long-term passive  
827 microwave satellite-based retrievals of vegetation optical depth. *Geophysical Research Letters*,  
828 38(18). doi: 10.1029/2011GL048684.

829 Liu, Y. Y., Dijk, A. I., McCabe, M. F., Evans, J. P., & Jeu, R. A. (2013). Global vegetation biomass  
830 change (1988–2008) and attribution to environmental and human drivers. *Global Ecology and*  
831 *Biogeography*, 22(6), 692-705. doi: 10.1111/geb.12024.

832 Liu, Y. Y., Van Dijk, A. I., De Jeu, R. A., Canadell, J. G., McCabe, M. F., Evans, J. P., & Wang, G. (2015).  
833 Recent reversal in loss of global terrestrial biomass. *Nature Climate Change*, 5(5), 470. doi:  
834 10.1038/nclimate2581.

835 Lucas, R. M., Mitchell, A. L., & Armston, J. (2015). Measurement of forest above-ground biomass  
836 using active and passive remote sensing at large (subnational to global) scales. *Current Forestry*  
837 *Reports*, 1(3), 162-177. doi: 10.1007/s40725-015-0021-9.

838 Luckman, A., Baker, J., Kuplich, T. M., Yanasse, C. D. C. F., & Frery, A. C. (1997). A study of the  
839 relationship between radar backscatter and regenerating tropical forest biomass for spaceborne  
840 SAR instruments. *Remote Sensing of Environment*, 60(1), 1-13. doi: 10.1016/S0034-  
841 4257(96)00121-6.

842 Meesters, A. G., De Jeu, R. A., & Owe, M. (2005). Analytical derivation of the vegetation optical  
843 depth from the microwave polarization difference index. *IEEE Geoscience and Remote Sensing*  
844 *Letters*, 2(2), 121-123. doi: 10.1109/LGRS.2005.843983.

845 Momen, M., Wood, J. D., Novick, K. A., Pangle, R., Pockman, W. T., McDowell, N. G., & Konings,  
846 A. G. (2017). Interacting Effects of Leaf Water Potential and Biomass on Vegetation Optical Depth.  
847 *Journal of Geophysical Research: Biogeosciences*, 122(11), 3031-3046. doi:  
848 10.1002/2017JG004145.

849 Morel, A. C., Saatchi, S. S., Malhi, Y., Berry, N. J., Banin, L., Burslem, D., ... & Ong, R. C. (2011).  
850 Estimating aboveground biomass in forest and oil palm plantation in Sabah, Malaysian Borneo  
851 using ALOS PALSAR data. *Forest Ecology and Management*, 262(9), 1786-1798. doi:  
852 10.1016/j.foreco.2011.07.008.

853 Myneni, R. B., Dong, J., Tucker, C. J., Kaufmann, R. K., Kauppi, P. E., Liski, J., ... & Hughes, M. K.  
854 (2001). A large carbon sink in the woody biomass of Northern forests. *Proceedings of the*  
855 *National Academy of Sciences*, 98(26), 14784-14789. doi: 10.1073/pnas.261555198.

856 NOAA. National Oceanic and Atmospheric Administration. (2017). ETOPO1 global relief model.  
857 Retrieved from: <https://www.ngdc.noaa.gov/mgg/global/global.html>

858 NSIDC. National Snow & Ice Data Center. (2017a). NASA Distributed Active Archive Center (DAAC)  
859 at NSIDC. EASE-Grid Data. Retrieved from: [http://nsidc.org/data/ease/ease\\_grid2.html](http://nsidc.org/data/ease/ease_grid2.html)

860 Owe, M., de Jeu, R., Holmes, T. (2008). Multisensor historical climatology of satellite-derived  
861 global land surface moisture. *Journal of Geophysical Research*, 113(F1). doi:  
862 10.1029/2007JF000769

863 Pan, Y., Birdsey, R. A., Fang, J., Houghton, R., Kauppi, P. E., Kurz, W. A., ..., & Ciais, P. (2011). A  
864 large and persistent carbon sink in the world's forests. *Science*, 1201609. doi:  
865 10.1126/science.1201609.

866 Pekel, J. F., Cottam, A., Gorelick, N., & Belward, A. S. (2016). High-resolution mapping of global  
867 surface water and its long-term changes. *Nature*, 540(7633), 418. doi:10.1038/nature20584.

868 Piles, M., Chaparro, D., Camps-Valls, G., Entekhabi, D., Konings, A. G., & Jagdhuber, T. (2017).  
869 Remote sensing of vegetation dynamics in agro-ecosystems using snap vegetation optical depth  
870 and optical vegetation indices. In: *Geoscience and Remote Sensing Symposium (IGARSS), 2017*  
871 *IEEE International* (pp. 4346-4349). IEEE.

872 Saatchi, S. S., Houghton, R. A., Dos Santos Alvala, R. C., Soares, J. V., & Yu, Y. (2007). Distribution  
873 of aboveground live biomass in the Amazon basin. *Global Change Biology*, 13(4), 816-837. doi:  
874 10.1111/j.1365-2486.2007.01323.x.

875 Saatchi, S. S., Harris, N. L., Brown, S., Lefsky, M., Mitchard, E. T., Salas, W., ... & Petrova, S. (2011).  
876 Benchmark map of forest carbon stocks in tropical regions across three continents. *Proceedings*  
877 *of the National Academy of Sciences*, 108(24), 9899-9904. doi: 10.1073/pnas.1019576108.

878 Simard, M., Pinto, N., Fisher, J. B., & Baccini, A. (2011). Mapping forest canopy height globally  
879 with spaceborne lidar. *Journal of Geophysical Research: Biogeosciences*, 116(G4).  
880 doi:10.1029/2011JG001708.

881 Sinha, S., Jeganathan, C., Sharma, L. K., & Nathawat, M. S. (2015). A review of radar remote  
882 sensing for biomass estimation. *International Journal of Environmental Science and Technology*,  
883 12(5), 1779-1792. doi: 10.1007/s13762-015-0750-0.

884 Sun, Z., Peng, S., Li, X., Guo, Z., & Piao, S. (2015). Changes in forest biomass over China during  
885 the 2000s and implications for management. *Forest Ecology and Management*, 357, 76-83. doi:  
886 10.1016/j.foreco.2015.08.013.

887 Teubner, I. E., Forkel, M., Jung, M., Liu, Y. Y., Miralles, D. G., Parinussa, R., ... & Camps-Valls, G.  
888 (2018). Assessing the relationship between microwave vegetation optical depth and gross  
889 primary production. *International Journal of Applied Earth Observation and Geoinformation*, 65,  
890 79-91. doi: 10.1016/j.jag.2017.10.006.

891 Thurner, M., Beer, C., Santoro, M., Carvalhais, N., Wutzler, T., Schepaschenko, D., ... & Schimmlus,  
892 C. (2014). Carbon stock and density of northern boreal and temperate forests. *Global Ecology*  
893 *and Biogeography*, 23(3), 297-310. doi: 10.1111/geb.12125.

894 Todd, S. W., Hoffer, R. M., & Milchunas, D. G. (1998). Biomass estimation on grazed and ungrazed  
895 rangelands using spectral indices. *International Journal of Remote Sensing*, 19(3), 427-438.

896 Ulaby, F. T., Moore, R. K., & Fung, A. K. (1986). Microwave remote sensing active and passive-  
897 Volume III: from theory to applications. Norwood, MA (USA): Artech House.

898 UNESCO. United Nations Educational, Scientific and Cultural Organization. (2017). World rivers.  
899 Retrieved from: [http://ihp-wins.unesco.org/layers/geonode:world\\_rivers](http://ihp-wins.unesco.org/layers/geonode:world_rivers).

900 Van Marle, M. J. E., Van Der Werf, G. R., de Jeu, R. A. M., & Liu, Y. Y. (2016). Annual South American  
901 forest loss estimates based on passive microwave remote sensing (1990-2010). *Biogeosciences*,  
902 13(2), 609-624. doi:10.5194/bg-13-609-2016.

903 Viet Nguyen, L., Tateishi, R., Kondoh, A., Sharma, R. C., Thanh Nguyen, H., Trong To, T., & Ho Tong  
904 Minh, D. (2016). Mapping tropical forest biomass by combining ALOS-2, Landsat 8, and field plots  
905 data. *Land*, 5(4), 31. doi:10.3390/land5040031.

906 Vittucci, C., Ferrazzoli, P., Kerr, Y., Richaume, P., Guerriero, L., Rahmoune, R., & Laurin, G. V.  
907 (2016a). SMOS retrieval over forests: Exploitation of optical depth and tests of soil moisture  
908 estimates. *Remote Sensing of Environment*, 180, 115-127. doi: 10.1016/j.rse.2016.03.004.

909 Vittucci, C., Ferrazzoli, P., Kerr, Y., Richaume, P., Guerriero, L., & Laurin, G. V. (2016b). SMOS forest  
910 optical depth intercomparisons over pan-tropical biomes. In Geoscience and Remote Sensing  
911 Symposium (IGARSS), 2016 IEEE International (pp. 5311-5314). IEEE. doi:  
912 10.1109/IGARSS.2016.7730383.

913 Vrije Universiteit Amsterdam (Richard de Jeu) & NASA GSFC (Manfred Owe). (2014).  
914 AMSR2/GCOM-W1 surface soil moisture (LPRM) L3 1 day 25 km x 25 km ascending V001.

915 Retrieved from: [https://disc.gsfc.nasa.gov/datacollection/LPRM\\_AMSR2\\_A\\_SOILM3\\_001.html](https://disc.gsfc.nasa.gov/datacollection/LPRM_AMSR2_A_SOILM3_001.html).  
916 doi: 10.5067/M5DTR2QUYLS2.

917 WWF. (2018). Seasonally flooded river basins of Brazil, Peru and Bolivia. Retrieved from:  
918 <https://www.worldwildlife.org/ecoregions/nt0128>.

919 Yuan, X., Li, L., Tian, X., Luo, G., & Chen, X. (2016). Estimation of above-ground biomass using  
920 MODIS satellite imagery of multiple land-cover types in China. *Remote Sensing Letters*, 7(12),  
921 1141-1149. doi: 10.1080/2150704X.2016.1219458.

922

**SUPPLEMENTARY FIGURES**

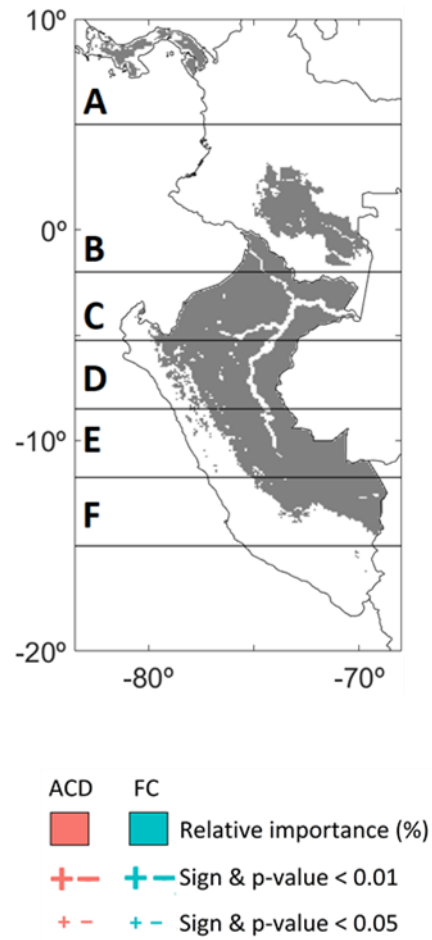
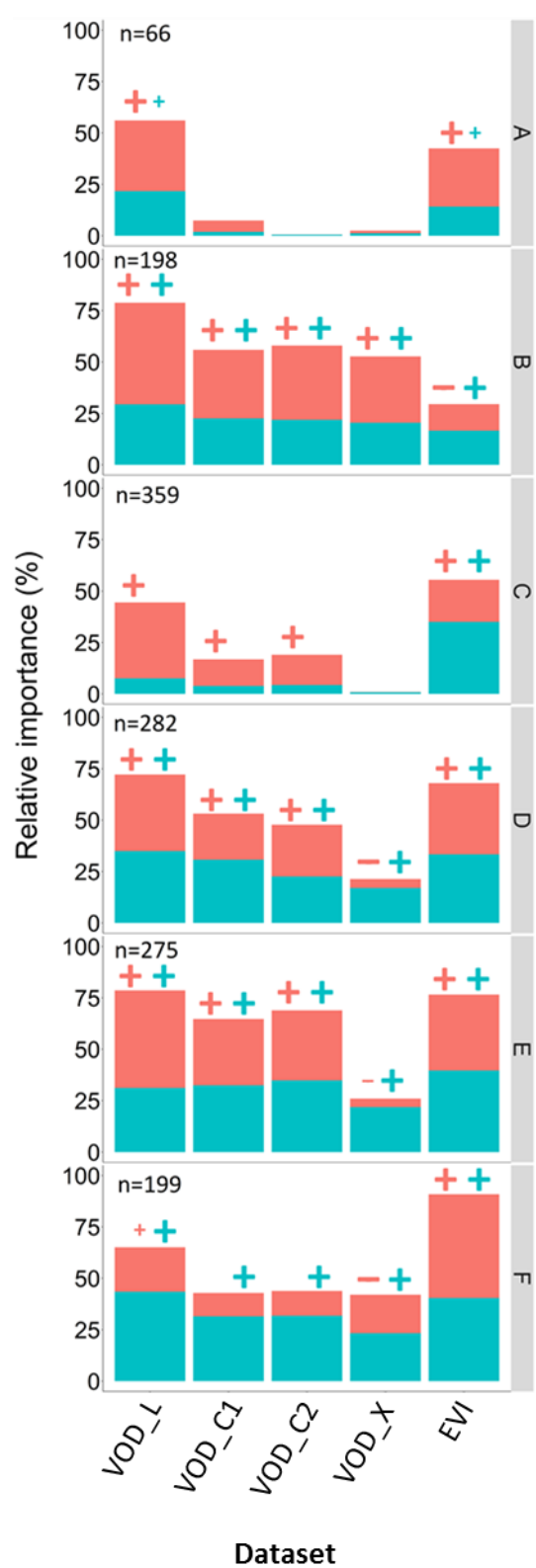
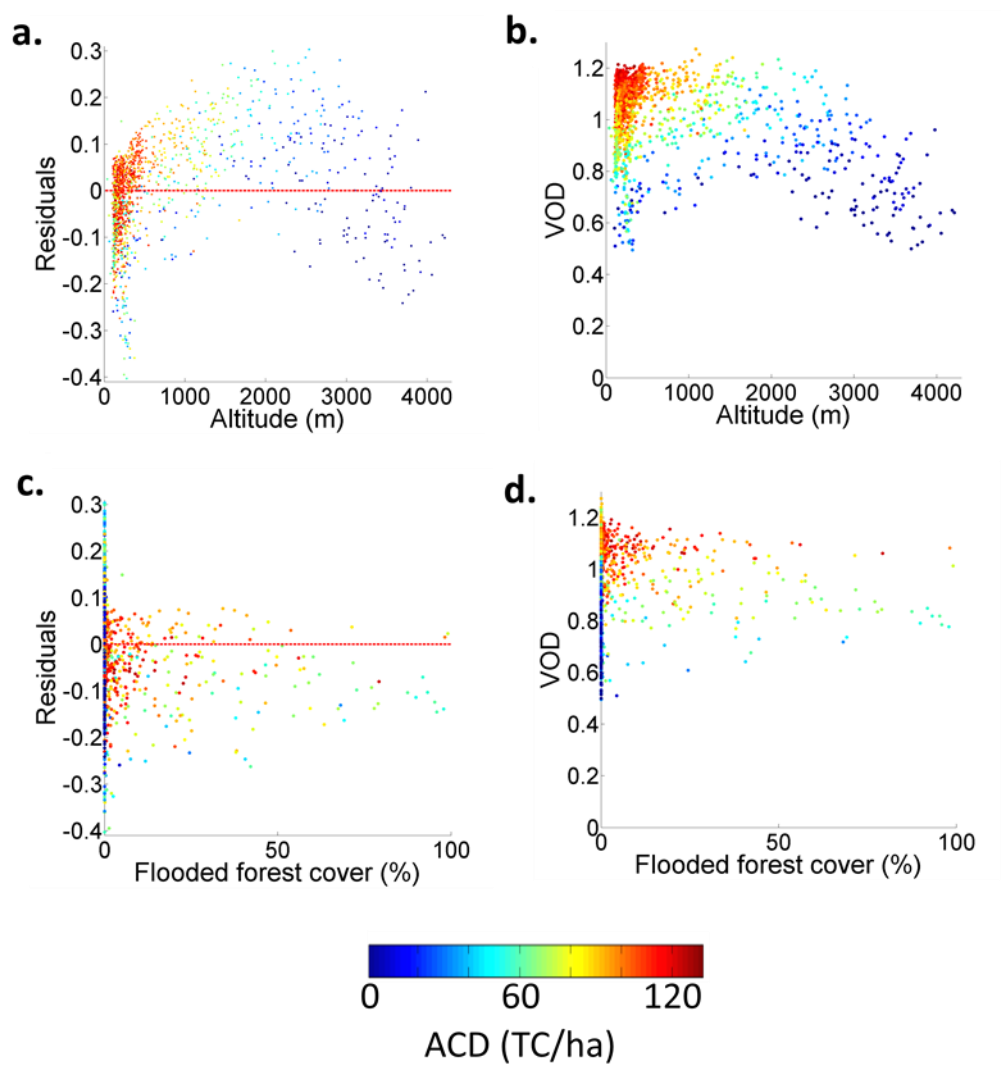


**Figure S1.** Relative importance of ACD and FC as predictors of VOD and EVI (Eq. (2)). Sign and significance for each variable are plotted if at least  $p < 0.05$ . Results are reported for regions (A) Panama, (B) Colombia and northern Peru, (C) north-central Peru, (D) central Peru, (E) south-central Peru and (F) southern Peru. Letter n refers to the sample.



927

928 **Figure S2.** Left column: relationship between residuals for the L-band VOD – ACD regression in  
929 Eq. (1) and: (a) altitude and (c) percentage of flooded forest. Dashed red lines show residuals  
930 equal to 0. Right column: relationship between L-band VOD and: (b) altitude and (d) percentage  
931 of flooded forest.

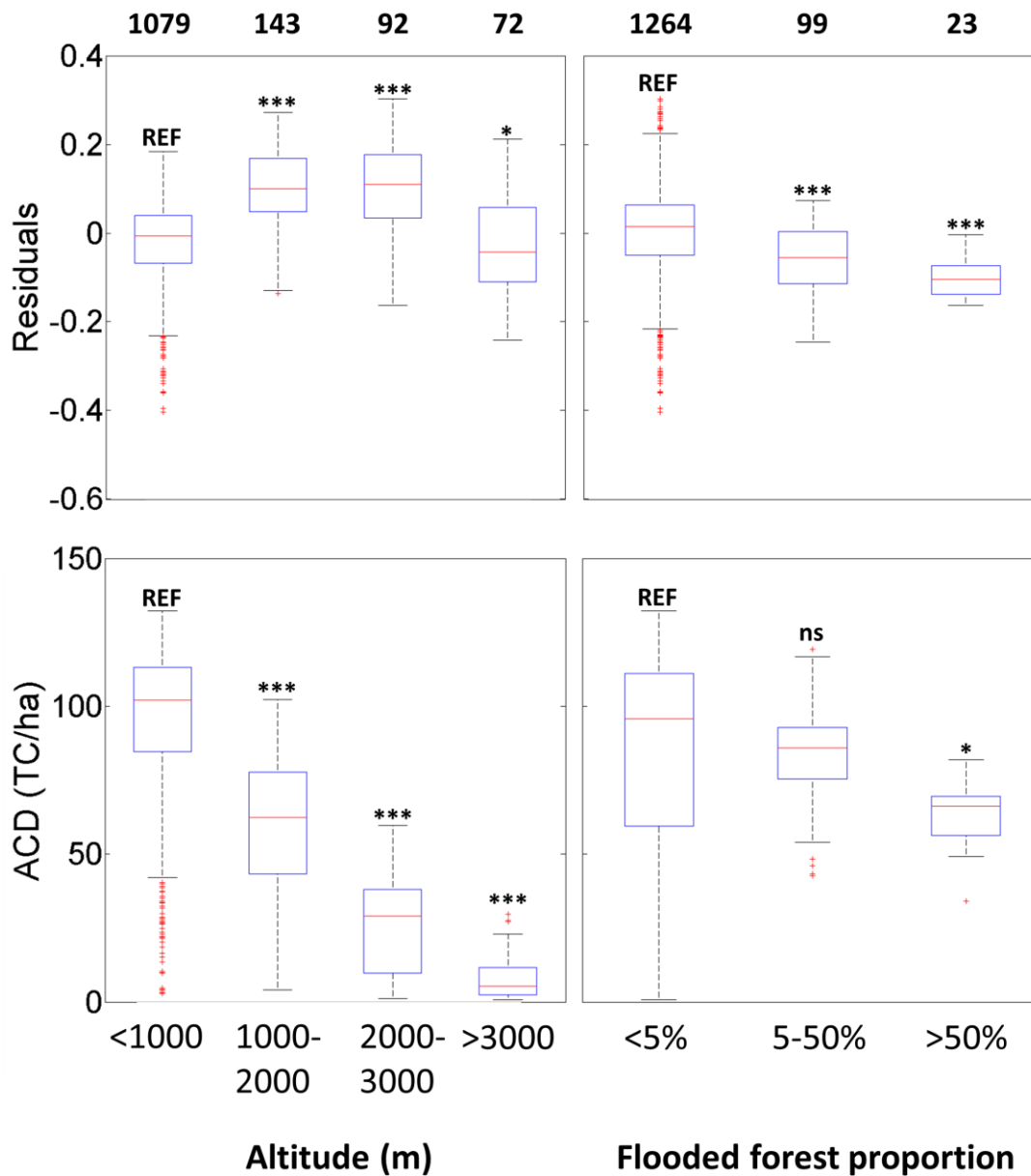


**Figure S3.** Residuals for model in Eq. (1) (top row) and ACD (bottom row) for different categories of altitude (left) and flooded forest proportion (right). It is tested if residuals are different from zero (top row), and if ACD for each group is different from the reference group (REF). Significance: REF (reference; not evaluated), ns ( $p > 0.05$ ), \* ( $p < 0.05$ ), \*\* ( $p < 0.01$ ), \*\*\* ( $p < 0.001$ ). Numbers above the graph show the sample for each group.



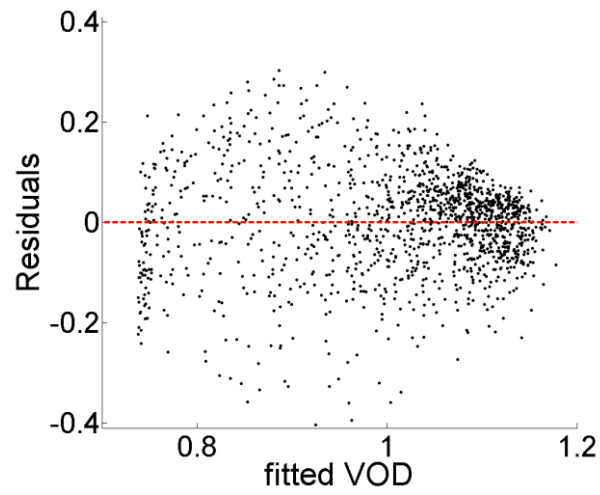


**Figure S4.** Fitted VOD values and residuals of VOD for the VOD-ACD linear regression.

## SUPPLEMENTARY TABLES

**Table S1.** Sample studied.

	Peru	Colombia	Panama	<b>Total</b>
All dataset	1,730	209	39	<b>1,978</b>
Only forests	1,152	198	36	<b>1,386</b>

**Table S2.** Results ( $R^2$  and significance) for the VOD-ACD regression in Eq. (1), applied to dense forests. Significance is shown as follows:  $p < 0.001$  (\*\*\*),  $p < 0.01$  (\*\*),  $p < 0.05$  (\*),  $p \geq 0.05$  (n.s.).

<b>Band</b>	<b>ACD category</b>	
	$\geq 80$ TC/ha	$\geq 100$ TC/ha
L (1.4 GHz)	0.12 (***)	0.05 (***)
C1 (6.9 GHz)	0.04 (***)	n.s.
C2 (7.3 GHz)	0.05 (***)	n.s.
X (10.7 GHz)	n.s.	n.s.